Joule

CellPress

Article

Asymmetric Temperature Modulation for Extreme Fast Charging of Lithium-Ion Batteries

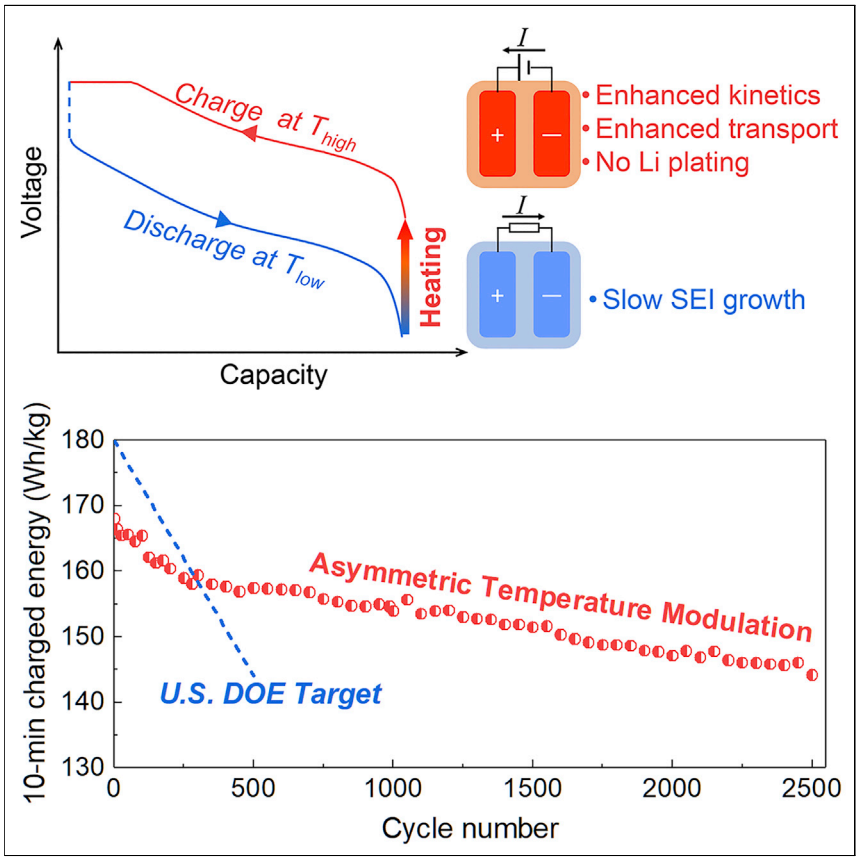

An asymmetric temperature modulation method is presented in which a Li-ion cell is rapidly pre-heated to and charged at ~60°C, and the cell's exposure time to 60°C is limited to ~10 min per cycle. The elevated temperature enhances kinetics and transport and hence eliminates Li plating; the limited exposure time to 60°C avoids severe materials degradation. We demonstrate that a high energy (209 Wh/kg) cell retains 91.7% capacity after 2,500 cycles of 10-min extreme fast charging, far exceeding the DOE target.

Xiao-Guang Yang, Teng Liu, Yue Gao, Shanhai Ge, Yongjun Leng, Donghai Wang, Chao-Yang Wang

cxw31@psu.edu

HIGHLIGHTS

Asymmetric charge and discharge temperatures enable durable extreme fast charging

High-temperature charging eliminates Li plating by enhanced transport and kinetics

Limited exposure time to high temperature avoids severe SEI growth

Elevated charging temperature reduces battery cooling need by >12×

Yang et al., Joule 3, 1–18
December 18, 2019
https://doi.org/10.1016/j.joule.2019.09.021

Please cite this article in press as: Yang et al., Asymmetric Temperature Modulation for Extreme Fast Charging of Lithium-Ion Batteries, Joule (2019), https://doi.org/10.1016/j.joule.2019.09.021

Joule

CellPress

Article

Asymmetric Temperature Modulation for Extreme Fast Charging of Lithium-Ion Batteries

Xiao-Guang Yang,[1,3] Teng Liu,[1,3] Yue Gao,[1] Shanhai Ge,[1] Yongjun Leng,[1] Donghai Wang,[1] and Chao-Yang Wang[1,2,4,*]

SUMMARY

Adding a 200-mile range in 10 min, so-called extreme fast charging (XFC), is the key to mainstream adoption of battery electric vehicles (BEVs). Here, we present an asymmetric temperature modulation (ATM) method that, on one hand, charges a Li-ion cell at an elevated temperature of 60°C to eliminate Li plating and, on the other, limits the exposure time at 60°C to only ~10 min per cycle, or 0.1% of the lifetime of a BEV, to prevent severe solid-electrolyte-interphase growth. The asymmetric temperature between charge and discharge opens a new path to enhance kinetics and transport during charging while still achieving long life. We show that a 9.5-Ah 170-Wh/kg cell sustained 1,700 XFC cycles (6 C charge to 80% state of charge) at 20% capacity loss with the ATM, compared to 60 cycles for a control cell, and that a 209-Wh/kg BEV cell retained 91.7% capacity after 2,500 XFC cycles.

INTRODUCTION

Range anxiety has long been cited as a major barrier to mainstream adoption of battery electric vehicles (BEVs).[1,2] The key to alleviating this anxiety is providing consumers with fast and convenient charging.[3] Governments and companies worldwide are pushing actively for a pervasive network of public direct-current fast chargers with the power recently elevated to 400 kW, targeting to add 200 miles of driving range in 10 min, the so-called extreme fast charging (XFC).[4] No BEV today, however, can withstand 400 kW.[5] The US Department of Energy (DOE) has identified several critical barriers to XFC in batteries, vehicles, and infrastructure and is dedicating resources to tackle them.[4] Regarding battery technology, specifically, the issue of Li plating and the overwhelming need for cooling during an XFC event are recognized by the DOE as the two most critical challenges.[6,7]

Current lithium-ion batteries (LiBs) predominantly utilize graphite as anode materials whose reversible potential is within 100 mV versus Li/Li^+. During charging, Li plating onto graphite surfaces competes with Li intercalation into graphite particles. To achieve a <10-min recharge, a charge rate of 6 C is needed. Such a high charge rate can induce large anode polarization, rendering Li plating thermodynamically favorable. A major symptom of Li plating is drastic capacity fade. Recent data[8] of 25 Ah automotive Li-ion cells showed that cell life, at 20% capacity loss, plummeted from >2,500 equivalent full cycles (EFCs) at 1 C charge to only ~200 EFCs at 4 C charge. Likewise, the 9.5 Ah graphite||$LiNi_{0.6}Mn_{0.2}Co_{0.2}O_2$ (NMC622) cells in this work can sustain >2,000 EFCs at 1 C charge and >1,500 EFCs at 3 C charge but only 50 EFCs at 6 C charge (Figure S1).

Context & Scale

Electric vehicles will only be truly competitive when they can be charged as fast as refilling a gas tank. The US Department of Energy has set a goal of developing extreme fast charging (XFC) technology that can add 200 miles of driving range in 10 min. A critical barrier to XFC is Li plating, which usually occurs at high charge rates and drastically deteriorates battery life and safety. Here, we present an asymmetric temperature modulation (ATM) method that charges a Li-ion cell at an elevated temperature of 60°C to eliminate Li plating and limits the exposure time to 60°C to only ~10 min per cycle to prevent serious materials degradation. Using industrially available battery materials, we show that a high-energy (209 Wh/kg) Li-ion cell with the ATM method retains 91.7% capacity after 2,500 XFC cycles (equal to 500,000 miles of driving range), far exceeding the US Department of Energy (DOE) target (500 cycles at 20% loss).

Li plating, fundamentally, is triggered due to a restricted rate of either of the following three physicochemical processes:[9–12] ion transport in the electrolyte, intercalation reaction at the interface of graphite and electrolyte, and solid-state diffusion in graphite particles. Consequently, research efforts in the literature have been focusing on: (1) enhancing ion transfer in the porous electrodes by optimizing electrolyte composition[13,14] or reducing electrode tortuosity;[15] (2) improving charge transfer kinetics through new electrolytes,[16,17] additives,[18] or coating graphite with amorphous nanolayers of silicon[19] or Al_2O_3;[20] (3) reducing solid-state diffusion resistance by adopting nano-materials;[21] and (4) searching for alternative anode active materials.[22–25] LiBs, however, are notorious for a "whack-a-mole" nature.[26] It is always challenging to improve one property without sacrificing others. For instance, Dahn and coworkers[13] reported that introducing esters like methyl acetate as co-solvents can improve electrolyte conductivity and reduce electrolyte viscosity, but the enhanced transport properties are mostly at the expense of electrolyte stability. Likewise, the super-concentrated electrolytes developed by Yamada et al.[16,17] enable excellent charge transfer kinetics at graphite surfaces, but their application in practical LiBs is hampered by the ultrahigh viscosity.

Recently, we present a thermal stimulation method that heats up a cell from a low ambient temperature to room temperature (RT) before charging, which enables durable 3.5 C charging of a 9.5-Ah, 170-Wh/kg graphite||NMC622 cell without Li plating at as low as −50°C.[27] The same cell under 6C XFC, however, would suffer severe Li plating and drastic capacity fade at RT (Figure S1). A potential method to suppressing Li plating under XFC is to further elevate charge temperature. Indeed, all the key parameters governing the aforementioned physicochemical processes are strong functions of temperature, following the Arrhenius law (Figure 1A). An increase of temperature, for instance from 20°C to 60°C, can boost graphite intercalation kinetics[28] by 13×, graphite solid-state diffusivity[29] by 5.6×, and electrolyte conductivity[30,31] by 1.9× simultaneously, thereby mitigating or eliminating Li plating. However, the increase of temperature is confronted by an accelerated solid-electrolyte-interphase (SEI) growth, which expedites lithium inventory loss. The cycle life of the 9.5-Ah graphite||NMC622 cells drops from >2,000 EFCs at RT to only ~250 EFCs at 60°C due to the aggravated SEI growth (Figure S2A). Hence, it is universally believed that LiBs have an optimum life at around RT[32,33] due to the interplay between Li plating and SEI growth (Figure S2) and therefore should avoid operating at high temperatures. Indeed, developing novel cooling methods to minimizing battery temperature rise during XFC is one of the technology gaps identified by the US DOE.[4,7]

Here, we present an approach that enables XFC of LiBs with excellent cycle life and, meanwhile, substantially reduces battery cooling need during XFC. The key idea is to solve the dilemma between enhanced performance and accelerated materials degradation at elevated temperatures through an asymmetric temperature modulation (ATM) method. That is, a cell is charged at a high temperature T_H (Figure 1B) to eliminate Li plating and, on the other hand, is exposed to T_H only in the fast-charging period, which is ~10 min per cycle. As SEI growth depends on time, the short exposure time to T_H prevents fatal SEI growth and hence effectively controls cell degradation. In the following, we select two types of mass-produced industrial electrodes to demonstrate the viability of this ATM approach in enabling XFC of today's LiBs without demanding new materials. We first employ the 9.5-Ah, 170-Wh/kg, graphite||NMC622 pouch cells for demonstration. By modulating cell temperature to charge at 60°C and discharge at around RT, the cells sustained 1,700 cycles of 6 C charge to 80% state of charge (SOC) at 20% capacity loss. For comparison, a

[1]Department of Mechanical Engineering, The Pennsylvania State University, University Park, PA 16802, USA

[2]EC Power, 341 Science Park Road, State College, PA 16803, USA

[3]These authors contributed equally

[4]Lead Contact

*Correspondence: cxw31@psu.edu

https://doi.org/10.1016/j.joule.2019.09.021

Please cite this article in press as: Yang et al., Asymmetric Temperature Modulation for Extreme Fast Charging of Lithium-Ion Batteries, Joule (2019), https://doi.org/10.1016/j.joule.2019.09.021

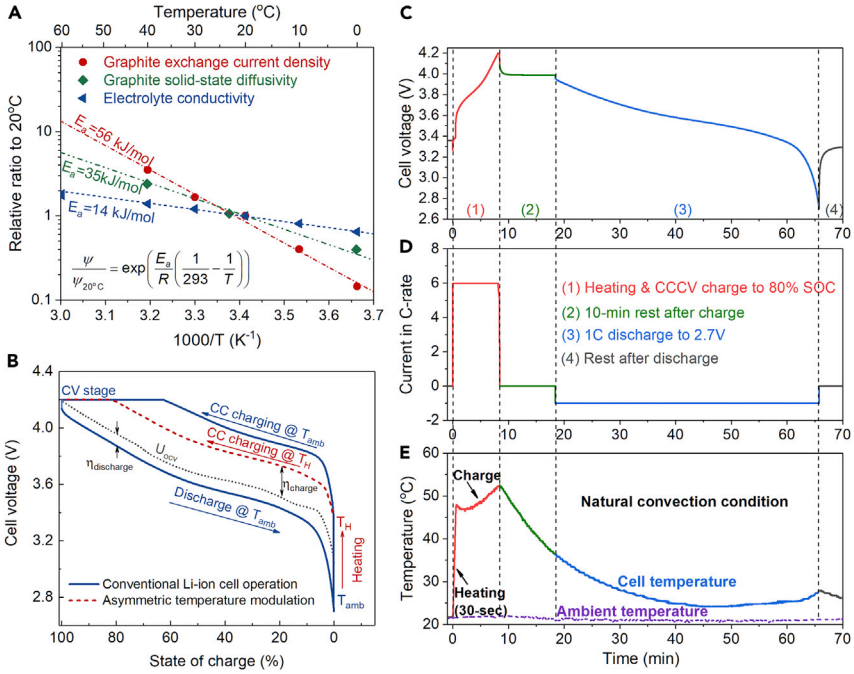

Figure 1. Asymmetric Temperature Modulation Method

(A) Enhancement ratio (relative to values at 20°C) of graphite exchange current density, graphite solid-state diffusivity, and electrolyte conductivity with the increase of temperature.

(B) Illustration of the asymmetric temperature modulation (ATM) method, which charges a cell at an elevated temperature T_H and discharges (and stores) the cell at the cool ambient temperature T_{amb}.

(C–E) Evolutions of (C) cell voltage, (D) current, and (E) temperature in an extreme fast charge cycle with ATM, which contains a heated CCCV (6 C, 4.2 V) charge at an average charge temperature of 49°C and 1 C discharge at an average temperature of 28°C. The cell was tested in ambient air without any forced convection.

control cell charged with 6 C directly at RT only survived 60 cycles. Meanwhile, we reveal that elevating the charge temperature, counterintuitively, reduces the cell cooling need in the 6 C charge process by >12×, owing to a smaller internal heat generation and an enlarged temperature difference driving heat dissipation. Finally, we select a BEV-type of electrodes having an anode loading of 2.94 mAh/cm^2 and a cell-level specific energy of 209 Wh/kg in a 35 Ah format. With ATM, the cell delivers a C/3 discharge energy of 167 Wh/kg after a 6 C charge to 80% SOC, close to the US DOE target of 180 Wh/kg. More profoundly, the BEV cell with ATM exhibits an outstanding cyclability, with only 8.3% capacity loss after 2,500 XFC cycles, far exceeding the US DOE target (500 cycles at 20% loss).

RESULTS AND DISCUSSION

Asymmetric Temperature between Charge and Discharge

Conventional LiBs are typically charged and discharged at a similar temperature (Figure 1B), depending on the ambient temperature and internal heat generation rate. The ATM method, as sketched in Figure 1B, takes active control of cell temperature in response to the most detrimental aging mechanism within the cell. That is, it elevates cell temperature during XFC to prevent Li plating and keeps the cell at the cool temperature during discharge (or storage) to suppress SEI growth. To elevate the charge temperature, we introduce a heated-charge protocol that adds a heating step to warm up the cell from ambient temperature (T_{amb}) to a high temperature (T_H)

Please cite this article in press as: Yang et al., Asymmetric Temperature Modulation for Extreme Fast Charging of Lithium-Ion Batteries, Joule (2019), https://doi.org/10.1016/j.joule.2019.09.021

prior to the conventional constant-current constant-voltage (CCCV) charging (Figure 1B). Heating speed is a crucial factor here as the total charging time including the heating step is limited to ~10 min. Conventional external heating methods face a dilemma between heating speed and uniformity, i.e., high heating rate leads to localized overheating near the cell surface[34]; their heating speed is thus restricted to <1°C/min, meaning that the heating step alone would already take far over 10 min. To shorten the heating time and achieve uniform heating, in this work we adopt the self-heating LiB structure,[35] which embeds thin nickel (Ni) foils inside a cell as internal heating elements, as sketched in Figure S3A. One end of the Ni foils is welded with anode tabs and connected to the negative terminal; the other end extends outside the cell to form a third terminal, the activation (ACT) terminal. A switch connects the positive and ACT terminals to navigate the input current. The Ni foils add only 1.3% weight and 0.47% cost to a conventional cell (see the calculation in Cell Materials and Fabrication). A control strategy is devised to implement the heated-charge protocol (Figures S3B and S3C). At the beginning, a charge current I is fed to the cell along with closing the switch between positive and ACT terminals. The Ni foil resistance R_{Ni} is specially tailored so that the product of I and R_{Ni} is close to open-circuit cell voltage U_{ocv}, i.e., $I \cdot R_{Ni} \approx U_{ocv}$. As such, most of the input current would flow into the Ni foils in the heating step without charging battery materials (Figure S3B). Once the cell is heated up to a desired temperature, the switch is opened to complete the heating step, and the cell is thereafter charged with the conventional CCCV protocol (Figure S3C).

We select the 9.5-Ah graphite||NMC622 pouch cells to demonstrate XFC with the ATM. These cells are designed for plug-in hybrid electric vehicles (PHEVs), with a cathode loading of 1.9 mAh/cm^2, an anode loading of 2.3 mAh/cm^2, and a specific energy of 170 Wh/kg. Hereafter, they are referred to as the PHEV cells to differentiate from the BEV cells presented later with a higher specific energy. Detailed design parameters of these cells are summarized in Table S1. Figures 1C–1E display the evolutions of cell voltage, current, and temperature in an XFC cycle with the ATM; an enlarged view of the heating and charge steps are presented in Figure S4. At first, a constant current of 57A (6 C) was fed to the cell together with closing the switch between positive and ACT terminals. During heating, almost all the current went into the Ni foils (Figure S4B), and the cell was charged by a negligible amount (0.018 Ah, or 0.19% SOC). The high current via the Ni foils created immense heat, warming up the cell from ~21°C to the defined temperature (45°C for Figure 1) in 30 s (a heating speed of 0.8°C/s). Thereafter, the heating step stopped by opening the switch and the cell was then charged with the 6 C current limited by a 4.2 V cutoff voltage until reaching 80% SOC. The total charging time, including the 30-s heating, amounted to 503 s, or 8.4 min.

It can be noted that cell temperature stayed between 48°C and 53°C during the charging step (Figure S4C). After being charged to 80% SOC, the cell rested at open circuit for 10 min and then discharged at a constant current of 1 C to 2.7 V. Cell temperature dropped rapidly in the rest and discharge steps (Figure 1E), though the cell was sitting in ambient air without any forced convection. The average cell temperature in the charge and discharge steps was 49°C and 28°C, respectively, clearly showing the asymmetry between charge and discharge temperatures.

Reduced Battery Cooling Need by Elevating Charge Temperature

Figure 2A compares the voltage profiles of three PHEV cells charged with the heated CCCV (6 C, 4.2 V) protocol at an average charge temperature of 40°C, 49°C, and 60°C, respectively, in addition to a control cell charged with CCCV (6 C, 4.2 V)

Please cite this article in press as: Yang et al., Asymmetric Temperature Modulation for Extreme Fast Charging of Lithium-Ion Batteries, Joule (2019), https://doi.org/10.1016/j.joule.2019.09.021

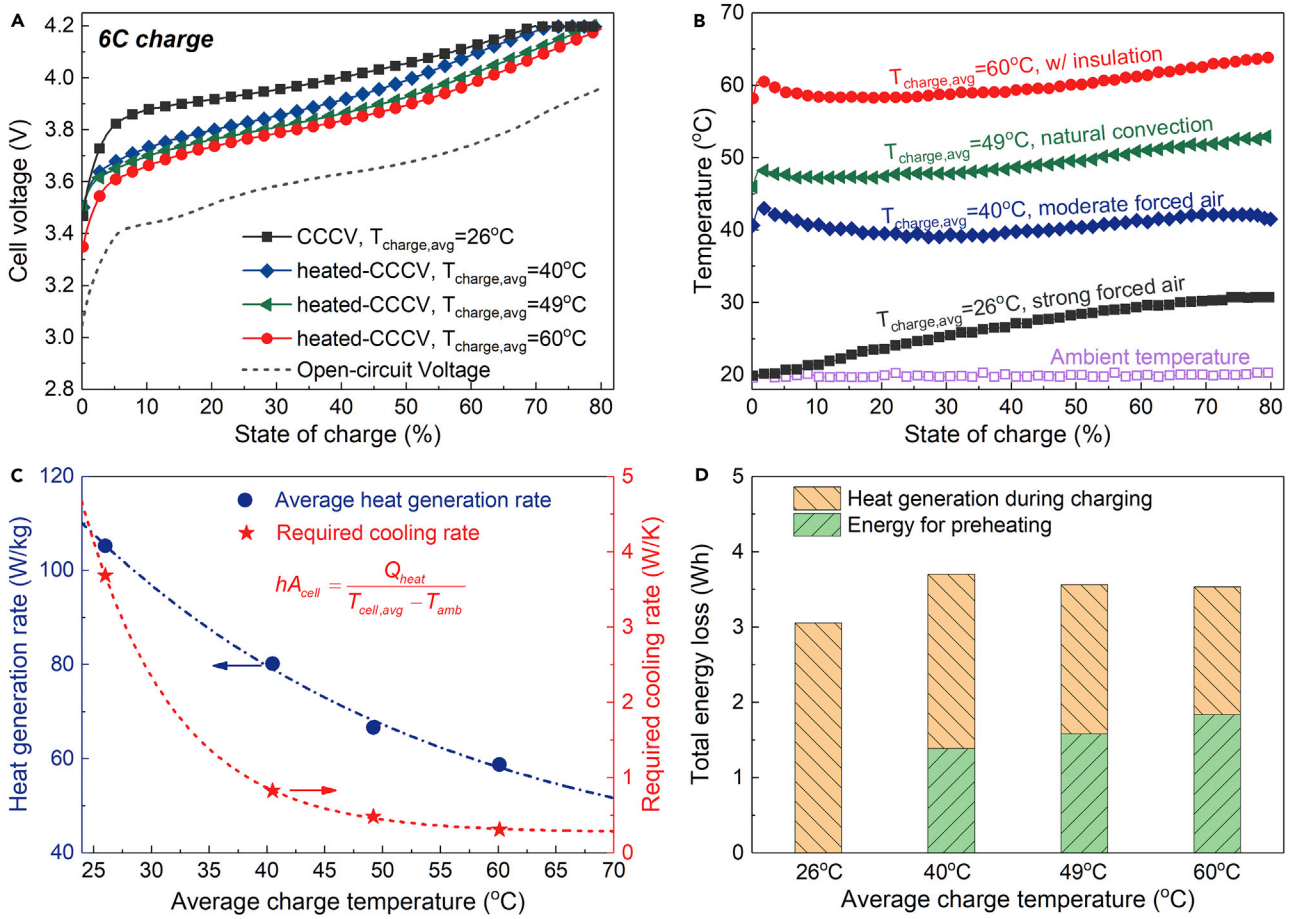

Figure 2. Reduced Cooling Need by Charging at an Elevated Temperature

(A and B) Evolutions of (A) cell voltage, and (B) cell temperature, in the CCCV (6 C, 4.2 V) charging process at an average charge temperature of 26°C, 40°C, 49°C, and 60°C, respectively. All the four PHEV cells were tested at an ambient temperature of ~20°C. The heated CCCV cells have a heating step before the CCCV charging. Different cooling conditions were applied to keep a relatively constant temperature during charging.

(C) Variation of the average heat generation rate in the charging process of the four PHEV cells and the required cooling need to balance the heat generation.

(D) Total energy loss to heat of the above four cells during the heating and charging processes. The four cells are the PHEV cells (see Table S1).

without preheating. All the tests were performed at an ambient temperature around 20°C, and different cooling strategies were applied to achieve a relatively constant temperature in the charging process (Figure 2B). Even though strong forced air by a fan was applied to the control cell, its temperature still rose by >10°C. With an increase of charge temperature, interestingly, the need for cooling is greatly reduced. Forced air at a lower air flow rate was sufficient to keep cell temperature at around 40°C, natural convection sufficed in the case of 49°C, and extra thermal insulation was required to maintain the cell temperature in the case of 60°C charging.

The cooling need during XFC can be quantitively estimated by the following energy balance ensuring zero cell temperature rise:

$$hA = \frac{I \cdot (V_{cell} - U_{ocv})}{T_{cell} - T_{amb}} \qquad \text{(Equation 1)}$$

where h is convective heat transfer coefficient and A is heat transfer surface area. It can be seen from Figure 2C (red line) that the average cooling need of the four PHEV

Please cite this article in press as: Yang et al., Asymmetric Temperature Modulation for Extreme Fast Charging of Lithium-Ion Batteries, Joule (2019), https://doi.org/10.1016/j.joule.2019.09.021

cells, calculated by Equation 1 with the voltage and temperature profiles in Figures 2A and 2B, drops exponentially with the increase of average charge temperature. The reason is 2-fold. On one hand, the term $I \cdot (V_{cell}-U_{ocv})$ which is heat generation rate (blue line in Figure 2C) is reduced by 1.3×, 1.6×, and 1.8×, respectively, as the average charge temperature increases from 26°C to 40°C, 49°C, and 60°C, owing to a smaller cell resistance at a higher temperature. On the other, the term $T_{cell}-T_{amb}$ is enlarged by 3.3×, 4.8×, and 6.7×, respectively, with T_{amb} of 20°C. Thereby, the overall cooling need during the XFC is reduced by 4.3×, 7.7×, and 12.1×, respectively, as the average charge temperature rises from 26°C to 40°C, 49°C, and 60°C. In addition, the reduced heat generation of charging at elevated temperatures partly compensates the energy consumption for preheating the cell before charging, as shown in Figure 2D. The total heat generation during the charging step is reduced from 3.05 Wh of the control cell to 1.7 Wh of the cell charged at 60°C. Hence, though it consumes additionally 1.83 Wh to preheat the cell from 20°C to 60°C before charging, the total energy loss to heat for charging at 60°C is only 0.48 Wh (1.36% of cell energy) higher than the control cell. We should also note that the energy for preheating comes from the external charger.

Enhanced Cyclability by Elimination of Li Plating at Elevated Charge Temperatures

Figure S5 displays the voltage profiles of the above four PHEV cells in the rest step subsequent to being charged to 80% SOC at different temperatures. A voltage plateau appeared for the control (26°C) and 40°C cells, leading to a local peak in the corresponding dV/dt plots (Figure 3A). The voltage plateau and dV/dt peak, as revealed in the literature,[36–38] indicate stripping of Li metal and appear only when Li plating is severe. As the average charge temperature increased to 49°C and 60°C, no voltage plateau or dV/dt peak was visible, suggesting that Li plating was, at least, substantially alleviated.

XFC cycling tests were performed following the protocols in Figures S6–S8. Each cycle consists of a heated CCCV (6 C, 4.2 V) charging to 80% SOC at a defined temperature, a rest step after charging, a 1 C discharge back to 2.7 V, and another rest step. Figure S9 displays the 1 C discharge capacity and Coulombic efficiency (CE) of the four cells during the cycling process. It is seen that the increase of charge temperature leads to higher CE and thereby longer cycle life. The cycling tests were paused periodically to calibrate cell capacity fade with a reference performance test (RPT), in which the cell was fully charged and then discharged at C/3 rate to 2.7 V (Figure S10). Figure 3B shows the retention of the C/3 discharge capacity in the RPTs of the four PHEV cells. The control cell without a preheating step lost 20% capacity in only 60 XFC cycles. With the increase of the charge temperature, the cycle life at 20% capacity loss increased to 380 cycles at 40°C, 1,000 cycles at 49°C, and 1,700 cycles at 60°C.

The remarkable boost of cycle life with the increase of charge temperature owes to the mitigation of Li plating. To confirm this, the four cells after the XFC cycling tests were fully discharged (C/3 to 2.7V) and then opened in a glove box for post-mortem analyses. Figures 3 and S11 present optical photos and scanning electron microscopy (SEM) images of the graphite anodes from the four aged cells. In the control cell (26°C), most part of the anode is covered by plated Li metal (Figure 3C), displaying a typical dendritic morphology[39] (Figure 3G). In the 40°C cell, the anode is covered by a thick film (Figure 3D), and graphite particles are hardly visible in the SEM image (Figure S11B). As the charge temperature increased to 49°C, the central part of the anode shows dark-blue color (Figure 3E), known as lithiated graphite in LiC_{18} phase;[40] SEM images from the dark-blue region present clear morphology

Please cite this article in press as: Yang et al., Asymmetric Temperature Modulation for Extreme Fast Charging of Lithium-Ion Batteries, Joule (2019), https://doi.org/10.1016/j.joule.2019.09.021

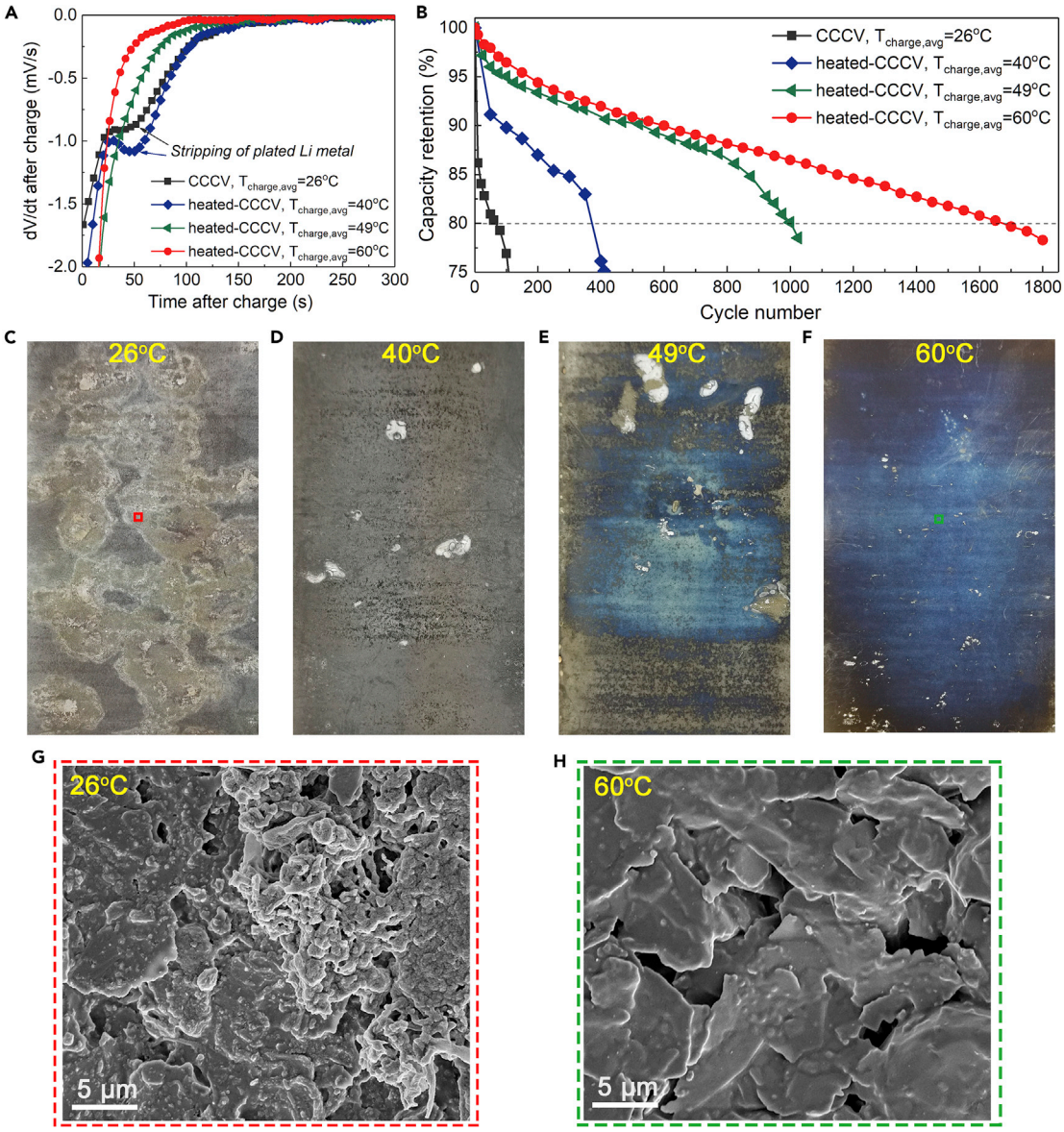

Figure 3. Enhanced Cycle Life by Mitigation of Li Plating at Elevated Charge Temperature

(A) Time derivative of voltage in the rest step subsequent to the CCCV (6 C, 4.2 V) charging to 80% SOC at different average charge temperatures (refer to Figure 2A). The peaks marked by arrows indicate stripping of plated Li metal (see also Figure S5).

(B) Capacity retention of the four PHEV cells during the XFC cycling test at different charge temperatures. The capacity refers to the C/3 discharge capacity in the reference performance test.

(C–F) Photos of the graphite anodes from the four cells after the XFC cycling test at the average charge temperature of (C) 26°C, (D) 40°C, (E) 49°C, and (F) 60°C.

(G and H) SEM images of the aged graphite anodes from the cell at (G) 26°C and (H) 60°C (see also Figure S11).

of graphite flakes (Figure S11C). Further elevating the charge temperature to 60°C, most part of the anode exhibits dark-blue color (Figure 3F), suggesting that Li plating was absent or minimal in this cell.

We then employed X-ray photoelectron spectroscopy (XPS) depth profiling to further confirm the existence of Li metal in the control cell and the elimination of Li plating in the 60°C cell, as shown in Figure 4A. The curves from top to bottom

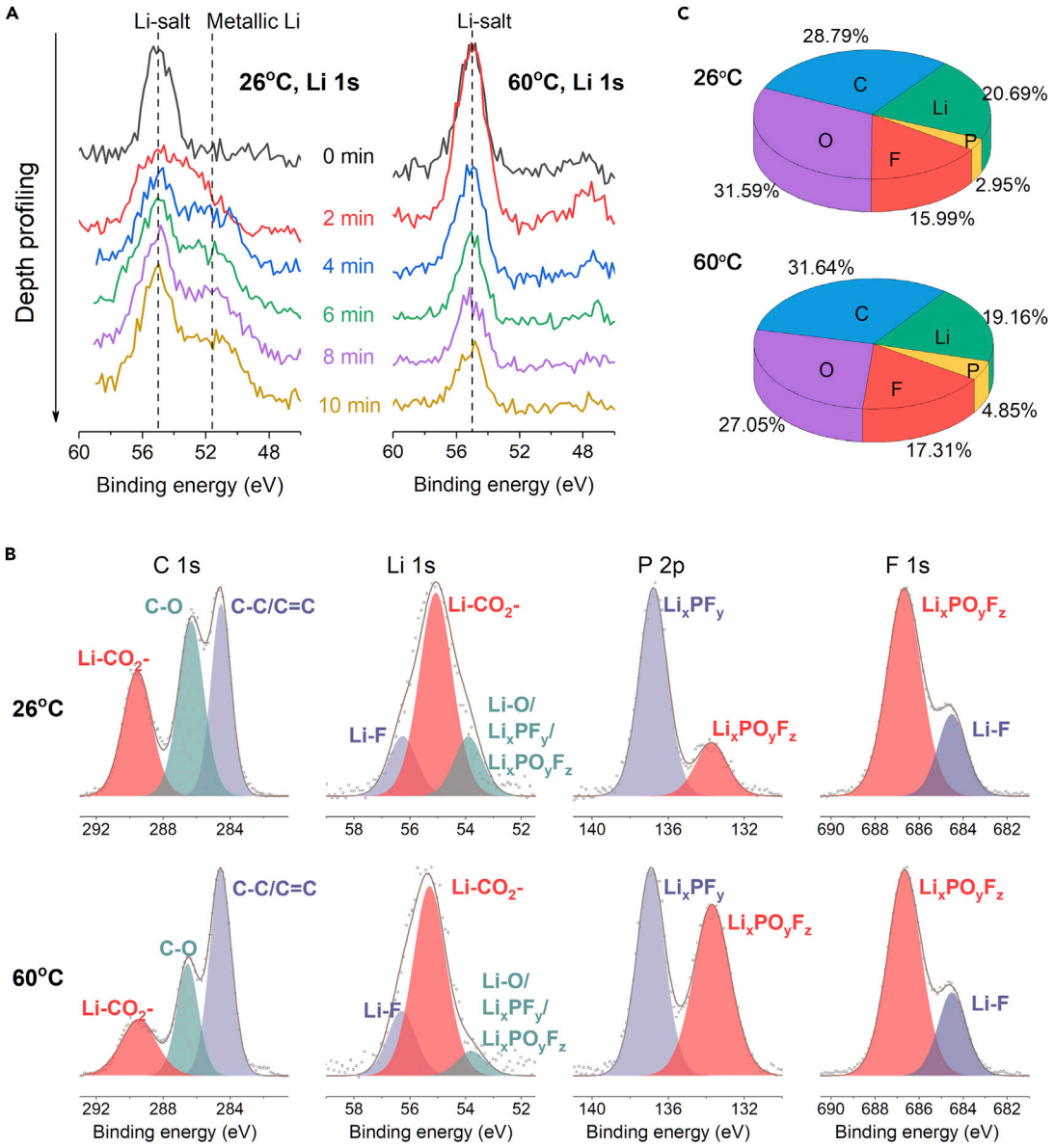

Figure 4. XPS Study of the Cells at Different Charge Temperatures

(A) XPS depth profiling of Li 1s spectra of the anode samples from the cells after XFC cycling test at the charge temperature of 26°C and 60°C. The sputtering speed is 30 nm/min based on SiO_2.

(B) High-resolution XPS spectra of C 1s, Li 1s, P 2p, and F 1s of the anode samples from the 26°C and 60°C cells.

(C) Elemental concentration of the anode samples from the 26°C and 60°C cells.

denote the Li 1s spectra acquired after sputtering for 0, 2, 4, 6, 8, and 10 min at a sputtering rate of 30 nm/min based on SiO_2. The top curve in both cases shows a peak at ~55 eV, which is associated with Li salts, indicating the top surface is covered by SEI. Starting from the 2nd curve, a new peak at ~51.5 eV corresponding to Li metal[41,42] appeared in the spectra of the 26°C cell, whereas no new peak appeared in the spectra of the 60°C cell.

We further performed high-resolution XPS to investigate the SEI structure of the cells at different charge temperatures, as presented in Figures 4B and S12. The XPS

Please cite this article in press as: Yang et al., Asymmetric Temperature Modulation for Extreme Fast Charging of Lithium-Ion Batteries, Joule (2019), https://doi.org/10.1016/j.joule.2019.09.021

spectra of the four cells show peaks with similar binding energies representative of typical components derived from a carbonate-based electrolyte. The peaks at 289.5 eV in the C 1s spectrum and 55.2 eV in the Li 1s spectrum denote Li-CO2-; the peaks at 56.3 eV in the Li 1s spectrum and 684.6 eV in the F 1s spectrum belong to LiF, and the peaks at 133.7 eV in the P 2p spectrum and 686.5 eV in the F 1s spectrum represent $Li_xPO_yF_z$.[41–43] Comparing the 26°C and 60°C cells (Figure 4B), we see two major differences in the concentrations of different SEI components: the concentration of Li-CO2- in the C 1s spectrum is higher in the 26°C cell than that in the 60°C cell, while the concentration of $Li_xPO_yF_z$ in the P 2p spectrum is higher in the 60°C cell than that in the 26°C cell. Figure 4C further compares the elemental concentrations of the two anode samples. It can be noted that the 60°C cell has higher concentrations of C, F, and P and lower concentrations of O and Li than that in the 26°C cell. The higher concentrations of P and F are likely due to the decomposition of $LiPF_6$ salt at the high temperature.

In the past, it was universally believed that LiBs should avoid operating at high temperatures due to the concern of accelerated side reactions such as severe SEI growth and salt decomposition. The remarkable boost of cycle life with the increasing charge temperature presented in Figure 3B, which is contrary to the conventional wisdom, suggests that the benefits of mitigated Li plating at the elevated temperature far outweigh the negative impacts associated with the exacerbated side reactions in the context of XFC. Indeed, the very slight increase in P and F concentrations in the 60°C cell (Figure 4C) indicates that $LiPF_6$ salt decomposition is effectively controlled. As will be discussed later, such manageable materials degradation owes to the limited exposure time to the high temperature.

It is worth mentioning that no voltage plateau or dV/dt peak was visible in the relaxation curves (Figures S5 and 3A) of the 49°C cell, though Li plating was locally observed in the photos of the aged anode (Figure 3E). In fact, the 49°C cell has faster capacity fade than the 60°C cell since the beginning of cycling (Figure 3B, the 49°C cell lost 5% capacity in 100 XFC cycles, compared to 3.5% loss of the 60°C cell). As the total capacity loss of a Li-ion cell is generally a sum of the capacity loss due to SEI growth and Li plating and SEI growth is deemed faster at 60°C than at 49°C, it can be inferred that Li plating occurred in the 49°C cell since the beginning of the XFC cycling. These results confirm the recent hypothesis[37,38] that voltage plateau can only be detected when a sufficient amount of Li is plated. An absence of voltage plateau signal is not necessarily indicative of a total absence of Li plating.

It should be noted that the rest step added between the charge and discharge steps in the cycling test is just a standard approach for testing of LiBs and is not an essential part of the ATM charging (drivers can drive the car immediately after charging). To demonstrate that the rest step has minimal impacts on the results presented herein, we performed 10 additional XFC cycles without a rest step between the heated 6 C charge at 60°C and 1 C discharge, followed by another 10 cycles with a 10-min rest step (see Figure S13). It can be seen that the voltage profiles are highly repeatable (Figure 5A); the temperature profiles of the cases with and without the rest step almost overlap in the time domain (Figure 5B) due to the small heat generation rate at 1 C discharge, and the 1 C discharge capacity over the 20 cycles is fairly stable (Figure 5C).

Mild SEI Growth by Limited Exposure Time to High Temperatures

To gain a deeper insight into the temperature effects on the interplay between Li plating and SEI growth, we make a further attempt to break down the capacity loss during the XFC cycling, as presented in Figure 6. The three PHEV cells under

Please cite this article in press as: Yang et al., Asymmetric Temperature Modulation for Extreme Fast Charging of Lithium-Ion Batteries, Joule (2019), https://doi.org/10.1016/j.joule.2019.09.021

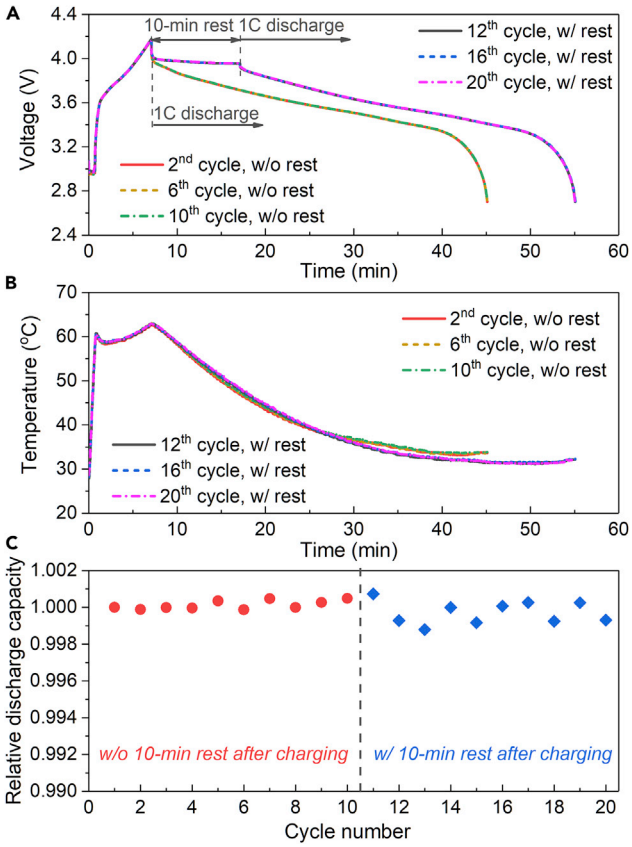

Figure 5. Negligible Impact of the Rest Step

(A and B) Voltage (A) and temperature (B) profiles of the cell cycled with a heated 6 C charge at 60°C and 1 C discharge with and without a 10-min rest step in between (see also Figure S13).

(C) Evolution of the 1 C discharge capacity (relative to the first cycle) in the 20 additional XFC tests. The first 10 cycles do not have the rest step after charging, and the second 10 cycles have a 10-min rest after charging.

XFC cycling with the ATM, referenced as ATM cells, are compared with three identical cells cycled with 1 C charge and 1 C discharge at an ambient temperature of 40°C, 50°C and 60°C, respectively, referenced as baseline cells. At a low charge rate of 1C and a temperature of >40°C, it is reasonable to assume an absence of Li plating. Thus, aging of the baseline cells is mainly ascribed to SEI growth. Various groups[44–46] have shown that SEI growth, at a particular temperature, is predominantly time dependent, following a $t^{1/2}$ dependence where t is the time from the beginning of cycling. As shown in Figures 6A–6C, the capacity retention (CR) of all the baseline cells can be fitted reasonably well using the following correlation having a $t^{1/2}$ dependence with a being a fitting parameter:

$$CR = 100 - a \cdot t^{1/2} \qquad \text{(Equation 2)}$$

which confirms that SEI growth dominates aging of the baseline cells. According to Dahn and coworkers,[46,47] plots of CR versus time for cells at the same temperature would fall on a same curve, irrespective of the cycling rate, if SEI growth is the main aging mechanism. On the other hand, a deviation from this curve is indicative of Li plating. Guided by this principle, we compare the CR plots of the ATM and baseline cells in the time domain (Figures 6A–6C). It should be mentioned that the baseline cells stayed at a high temperature throughout the cycling process, while the ATM

Please cite this article in press as: Yang et al., Asymmetric Temperature Modulation for Extreme Fast Charging of Lithium-Ion Batteries, Joule (2019), https://doi.org/10.1016/j.joule.2019.09.021

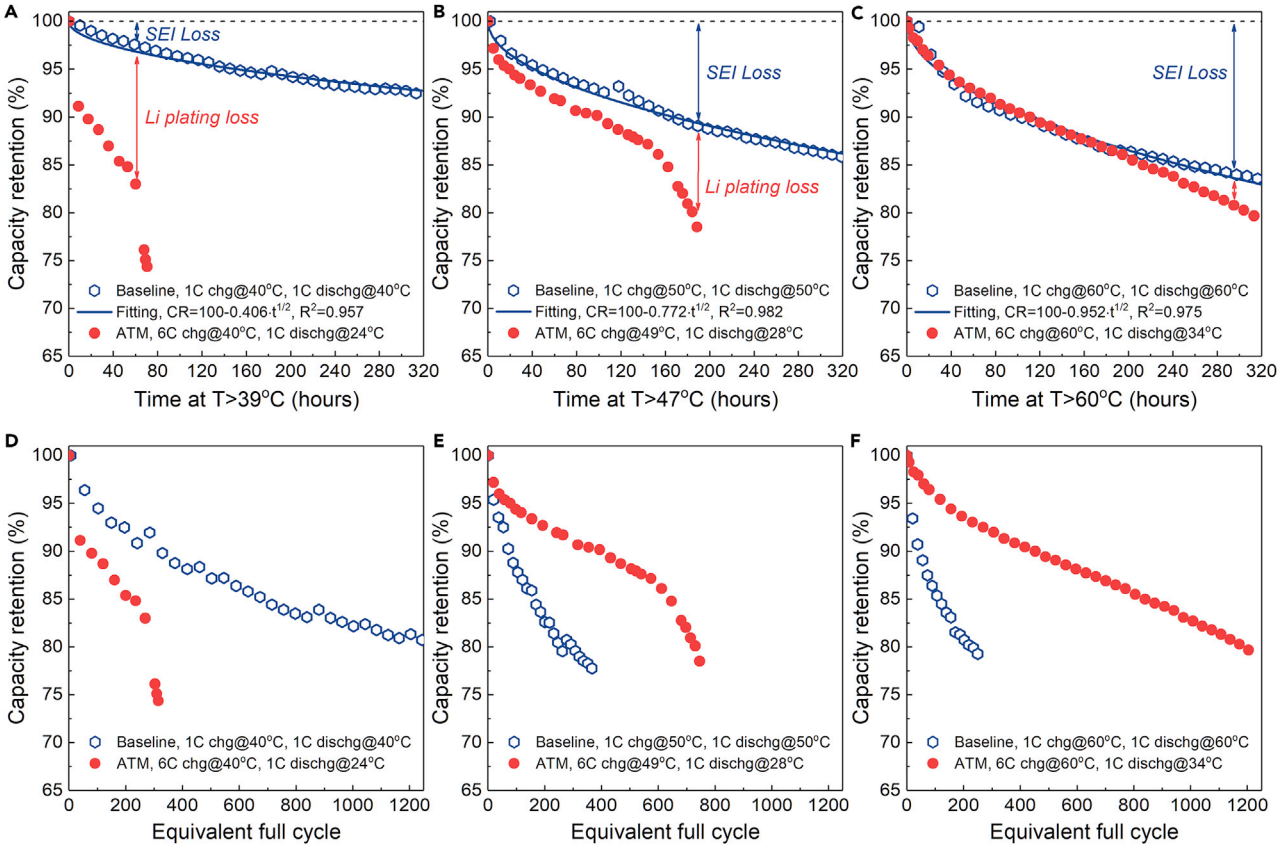

Figure 6. Solution to the Dilemma between Li Plating and SEI Growth

(A–C) Capacity retention versus time. The baseline cells are cycled with 1 C charge and 1 C discharge at a controlled temperature of (A) 40°C, (B) 50°C, and (C) 60°C, respectively. The ATM cells are cycled with 6 C charge at a high temperature and 1 C discharge at around room temperature (see the legends for the average charge and discharge temperatures). Capacity retention of the baseline cell can be fitted well with a correlation depending on the square root of time (the solid lines in A–C), meaning that SEI growth is the major aging mechanism. The difference between the ATM and baseline cells in the time domain (A–C) is owing to Li plating, which is substantially alleviated by elevating the charge temperature (see also Figure S14).

(D–F) Capacity retention versus equivalent full cycle of the ATM and baseline cells at the temperatures of (D) 40°C, (E) 50°C and (F) 60°C. The ATM cells are exposed to a high temperature only for ~10 min per cycle, thereby having much longer cycle life (in E and F) than the baseline cells that stay at the high temperatures throughout cycling. All the cells in this figure are the PHEV cells (see Table S1).

cells were exposed to a high temperature only for a small fraction of time in each cycle. To make a reasonable comparison, the time of the ATM cell in Figure 6 is defined as the duration in which cell temperature is above the minimum temperature during the charging step, thereby including the entire charging period plus a small fraction of the subsequent rest step in each cycle (see Figures S6–S8). It is highly interesting to note that the CR plots of the ATM and baseline cells at 60°C (Figure 6C) overlap in the first 160 h of cycling, meaning that charging at 60°C eliminates Li plating at 6 C charge. It also suggests that SEI growth in the 10-min charging period of the ATM cell in which the cell is at ~60°C far exceeds the SEI growth in the rest and discharge steps where the cell is at cooler temperatures. With the decrease of charge temperature (Figures 6A and 6B), CR of the ATM cell drops much faster than the baseline cell, reflecting a more severe Li plating at a lower charge temperature. According to Dahn and coworkers,[46,47] capacity loss of the baseline cell in each of these figures can be treated as the SEI-induced loss at this particular temperature, and the difference between the ATM and baseline cells reflects Li-plating-induced loss. As such, the contributions of SEI growth and Li plating to the total capacity loss can be deconvoluted (see Figure S14). Clearly, an increase in charge temperature, though

accelerating SEI growth (Figure S14A), significantly mitigates Li plating (Figure S14B) and thereby enhances the overall cyclability under XFC.

It is worth mentioning that all the cells under the XFC cycling tests exhibited a rapid capacity fade after a certain number of cycles (Figure 3B); the lower the average charge temperature, the earlier the onset of the transition. This nonlinear capacity fade, so-called "capacity rollover," is reportedly attributed to two possible causes: a dramatic rise of Li plating rate due to clogging of anode pores[48,49] or an abrupt increase of cathode impedance.[50,51] For the cells in this work, we believe that the capacity rollover owes to the former cause given the following observations. First, the ATM cell charged at 49°C switched to cycling with 1 C charge after the XFC cycling, and capacity fade immediately stabilized (Figure S15), meaning that the capacity rollover is strongly related to charge rate (i.e., high charge rate leads to more serious Li plating). Second, the optical and SEM images of the aged 40°C cell (after the capacity rollover) do show thick films covering the anodes and clogging the pores (Figures 3D and S11B). Third, electrochemical impedance spectroscopy (EIS) tests showed no abrupt increase of cell impedance over cycling (Figure S16). The high frequency resistance was stable (Figure S16E) and the charge transfer resistance increased linearly with cycle number (Figure S16F).

Figures 6D and 6E compare the ATM and baseline cells in terms of CR versus EFC. It is interesting to note that the baseline cell, which stayed at 60°C throughout cycling with 1 C charge and discharge, only sustained 250 EFCs at 20% capacity loss, whereas the ATM cell, which was exposed to 60°C only in the 6 C charge step, achieved an excellent life of 1,200 EFCs (Figure 6F). Even for the two cells at around 50°C (Figure 6E), cycle life of the ATM cell is 2.4× of the baseline cell (730 versus 300 EFCs). Such a remarkable boost of cycle life underscores an intrinsic superiority of the asymmetric temperature operation; that is, it enjoys the benefits of enhanced kinetics and transport by elevating the charge temperature while maintaining a manageable degradation rate through the limited exposure time to high temperature. Indeed, the ATM method only exposes a cell to a high temperature for ~10 min per cycle, or 7 days per 1,000 cycles. Assuming each fast charge adds 200 miles of driving range, 1,000 cycles would amount to 200,000 miles of driving range and further to 14.8 years of BEV operation based on the statistic data that Americans drive an average of 13,476 miles per year.[52] In other words, the ATM method only exposes a BEV to the high temperature for 0.1% of its lifetime (7 days out of 14.8 years).

Exceptional Cycle Life of High-Energy BEV Cells with Low-BET Area Anodes

With the elimination of Li plating, aging of the ATM cell is mainly due to SEI growth in the 10-min charging step during which the cell is at 60°C. Mitigating SEI growth at the high temperature is the key to further enhancing cell life. As shown by Dahn and coworkers,[46] SEI-induced capacity loss is proportional to the anode specific surface area, or the Brunauer-Emmett-Teller (BET) area. Hence, we select a BEV-type graphite anode having a BET area of 1.5 m^2/g (compared to 3.9 m^2/g of the PHEV anodes) at a loading of 2.94 mAh/cm,[2] along with a BEV-type cathode using $LiFePO_4$(LFP)-coated $LiNi_{0.5}Mn_{0.3}Co_{0.2}O_2$ (NMC532) at a loading of 2.55 mAh/cm,[2] and fabricated 10.5 Ah pouch cells using the self-heating LiB structure.

XFC test of the BEV cell was performed with a heated CCCV charge at an average charge temperature of ~61°C (Figure S17). The cutoff voltage was lowered to 4.15 V to protect cathode materials according to the materials supplier's instruction. Despite the lowered cutoff voltage, the BEV cell can still be charged to 80% SOC

Please cite this article in press as: Yang et al., Asymmetric Temperature Modulation for Extreme Fast Charging of Lithium-Ion Batteries, Joule (2019), https://doi.org/10.1016/j.joule.2019.09.021

in <10 min (Figure S17). XFC cycling test was conducted following the procedures in Figure S18 and was paused every 50 cycles for calibration of capacity fade. In the first cycle of each 50 consecutive XFC cycles, the cell charged to 80% SOC was discharged at C/3 to 2.7 V to quantify the fast charged specific energy, which refers to the deliverable energy at C/3 rate that one fast charge to 80% SOC can enable, a pivotal metric for evaluating fast charging capability proposed by the US DOE. In the remainder 49 XFC cycles of each 50 consecutive cycles, to save the overall test time, the cell after charging was first discharged at 1 C to 2.7 V, followed by a second discharge at C/3 to 2.7 V.

The BEV cell exhibits a remarkable stability at 60°C, as shown in Figure 7A, where, similar to Figure 6C, the BEV cell with the ATM (heated CCCV charge at 61°C and 1 C discharge at 27°C) is compared to a baseline BEV cell with 1 C charge and 1 C discharge both at 60°C. We can see that CR of the two cells fall on the same curve in the time domain, demonstrating once again that elevating charge temperature to 60°C eliminates Li plating and makes cell aging dominated by SEI growth in the charge period. Comparing Figures 7A and 6C, we can learn that the BEV cells degrade much slower than the PHEV cells (5.5% capacity loss after 300 h, compared to 19.7% loss of the PHEV cells). The superior high-temperature stability of the BEV cells owes largely to the low anode BET area, which is 2.6× smaller than the PHEV anodes. As shown in Figure S19B, the capacity losses of the PHEV and BEV cells become fairly close to each other when the capacity loss is normalized by the total graphite surface area, suggesting that anode BET area is a crucial factor for SEI-induced aging. The slightly higher area-normalized capacity loss of the PHEV cell than the BEV cell possibly originates from a larger cathode degradation in the PHEV cells, as the BEV cells employ LFP-coated NMC532 as the cathode materials and the olivine-phase coating layer on NMC surfaces can effectively mitigates cathode degradation by suppressing transition metal dissolution[53] and structure evolution (from layered to spinel and to rock salt).[54]

With the remarkable high-temperature stability, the BEV cell with ATM retains 91.7% of its initial capacity after 2,500 cycles of 6 C charge to 80% SOC (Figure 7B). In addition, the total charge time increases only marginally upon cycling (Figure 7C). Even after 2,500 XFC cycles, the cell can still be charged to 80% SOC in <12 min. The increase of charge time owes to the increased cell resistance, leading to a longer constant-voltage charge period (Figure S20).

The overarching target of the US DOE on XFC is to achieve a fast charged specific energy of 180 Wh/kg at the beginning of life (BOL) along with a life of >500 cycles at 20% loss. To estimate the cell-level specific energy that the BEV-type electrodes can deliver in practical automotive battery configurations, we fabricated a large-format 35 Ah cell using the same electrodes, which gives a C/3 specific energy of 209 Wh/kg (compared to 183 Wh/kg of the 10.5 Ah cell). Hence, the fast charged specific energy of the 10.5 Ah BEV cell, measured in the first cycle of each 50 consecutive XFC cycles, is multiplied by a ratio of 1.14 (209 Wh/kg over 183 Wh/kg) to estimate the fast charged specific energy in the 35 Ah format, as displayed in Figure 7D. The DOE target is also added for comparison (dashed line in Figure 7D). It can be seen that the BEV cell in the 35 Ah format achieves a fast charged specific energy of 167 Wh/kg at the BOL, which is 7% lower than the 180 Wh/kg DOE target. Nevertheless, the extraordinary cycling stability of the BEV cell makes it surpass the DOE target in 300 XFC cycles. Even after 2,500 XFC cycles, the BEV cell still retains a fast charged specific energy of 144 Wh/kg (equal to the DOE target at 500 cycles), indicating a boost of DOE target on cycle life by 5×.

Please cite this article in press as: Yang et al., Asymmetric Temperature Modulation for Extreme Fast Charging of Lithium-Ion Batteries, Joule (2019), https://doi.org/10.1016/j.joule.2019.09.021

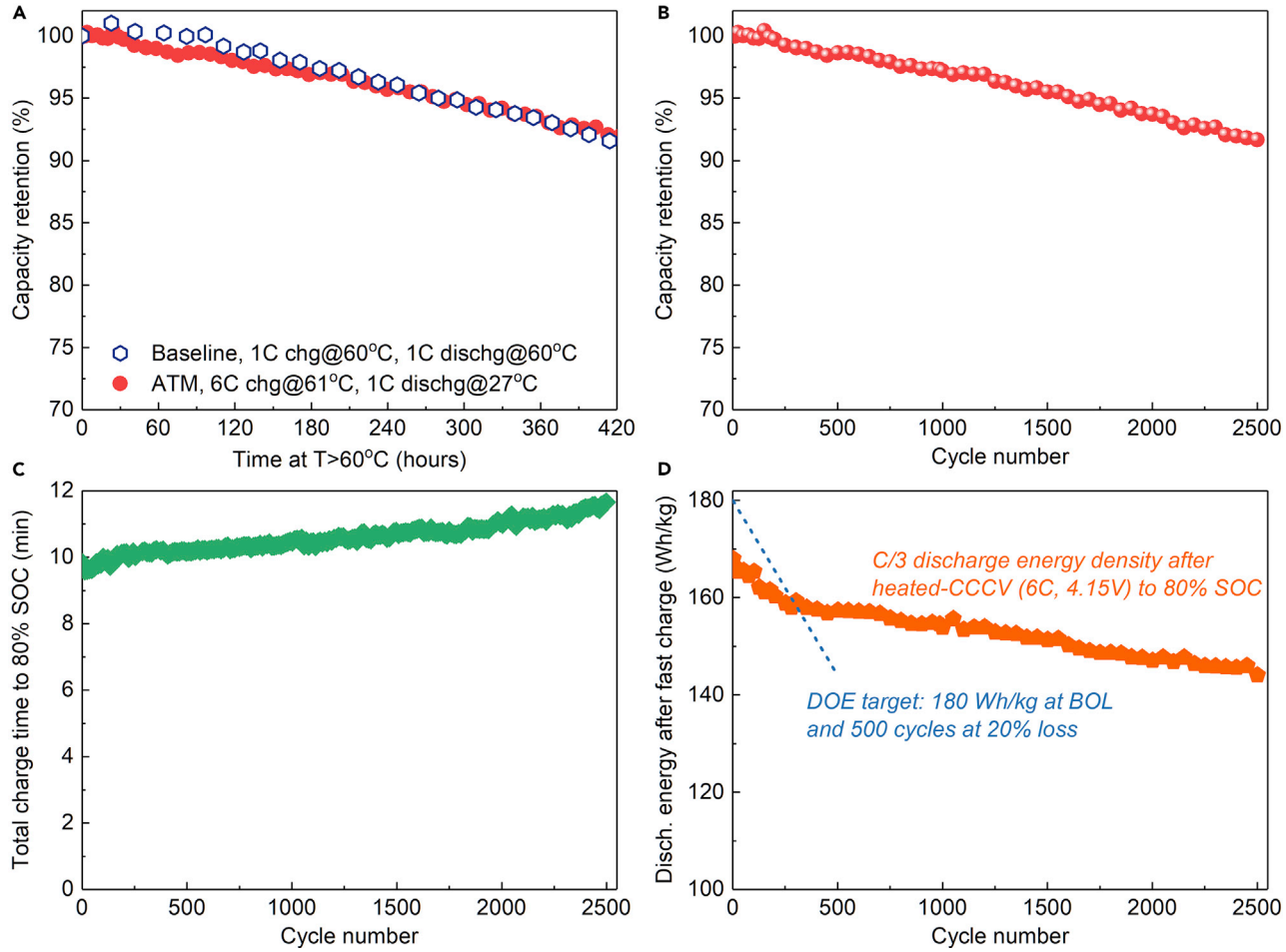

Figure 7. Extraordinary Cyclability of High-Energy BEV Cells Using Graphite with Low Specific Surface Area

(A) Capacity retention versus time. The two cells are identical. The baseline cell was cycled with 1 C charge and 1 C discharge always at 60°C, while the asymmetric temperature modulation (ATM) cell was cycled with 6 C charge at an average cell temperature of 61°C and 1 C discharge at an average cell temperature of 27°C. The overlap of the two profiles indicates SEI-dominated aging (i.e., no Li plating during 6 C charge of the ATM cell). The two BEV cells have markedly superior capacity retention than the PHEV cells in Figure 5C due to the use of graphite with a lower BET area, which alleviates SEI growth (see also Figure S19).

(B) Capacity retention of the ATM cell versus cycle number. The cell retained 91.7% of initial capacity after 2,500 cycles of 6 C charge from 0% to 80% state of charge (SOC).

(C) Evolution of the total charge time in each cycle (including a heating step that warms up the cell from ambient temperature to ~60°C).

(D) Evolution of the fast charged specific energy, referring to the specific energy of the C/3 discharge process subsequent to 6 C charging to 80% SOC, of the BEV cell in 35-Ah format. The dashed line is the target of XFC set forth by the US Department of Energy (DOE).

Assuming that each XFC adds 200 miles of driving range, the results in Figure 7 indicate that the BEV cell, with the ATM, retains 91.7% of its capacity and 86.2% of its fast charged specific energy after 500,000 miles of driving. To the best of our knowledge, this is the best cycle life reported so far in the context of XFC. Furthermore, all the cells in this work are based on industrially mass-produced electrodes and standard electrolyte (1M $LiPF_6$ in EC/EMC [3:7 by wt.] + 2 wt % VC), amply proving that the presented ATM method can enable XFC of today's BEVs with minimal changes required.

In broad perspectives, the scientific merit of the ATM is that it offers a solution to expediting electrochemical processes (e.g., enhancing kinetics and transport) while still effectively managing materials degradation. For battery applications, the

Please cite this article in press as: Yang et al., Asymmetric Temperature Modulation for Extreme Fast Charging of Lithium-Ion Batteries, Joule (2019), https://doi.org/10.1016/j.joule.2019.09.021

discharge profiles depend on the end-users, while the charging protocol is defined by manufacturers and thus can be specially designed and controlled. The ATM method presented herein opens a new path for designing electrochemical energy systems that can achieve high performance and long life simultaneously.

Conclusions

Over the decades, it is universally believed that LiBs should avoid operating at high temperatures due to the concern of accelerated materials degradation. In contrary to this conventional wisdom, we present an ATM method that charges a cell at an elevated temperature of 60°C and discharges (and stores) the cell at a cool temperature. The limited exposure time to 60°C (~10 min per cycle, or 0.1% of the lifetime of a BEV) effectively eliminates Li plating thanks to the enhanced kinetics and transport while still maintaining a mild SEI growth. Using industrially available battery materials, we demonstrate that the ATM enables durable XFC of today's LiBs with minimal changes required. The cycle life of a 9.5-Ah, 170-Wh/kg cell under XFC (6 C charge to 80% SOC) increases from 60 cycles to 1,700 cycles as the average charge temperature rises from 26°C to 60°C, clearly showing the benefits of elevated charge temperature. In addition, charging at 60°C reduces the battery cooling need by >12× due to a smaller heat generation rate and an enlarged temperature difference driving heat dissipation. Furthermore, we reveal that cell aging with the ATM depends primarily on SEI growth in the 10-min charging period. Employing graphite with a low-BET area to suppress SEI growth, a high-energy BEV cell having a C/3 specific energy of 209 Wh/kg in a 35-Ah format exhibits an outstanding cyclability, with only 8.3% capacity loss after 2,500 XFC cycles, the best cycle life reported so far in the context of XFC which far exceeds the US DOE target.

EXPERIMENTAL PROCEDURES

Cell Materials and Fabrication

Two types of mass-produced industrial electrodes are selected for cell fabrication in this work. The first type is designed for plug-in hybrid electric vehicles (PHEVs), referred to as PHEV cells, and the second type is for BEVs, referenced as BEV cells. The PHEV cells use $LiNi_{0.6}Mn_{0.2}Co_{0.2}O_2$ (NMC622) as cathode materials at a loading of 10.57 mg/cm^2, or 1.9 mAh/cm^2, and artificial graphite with a BET area of 3.9 m^2/g as anode materials at a loading of 6.68 mg/cm^2, or 2.33 mAh/cm^2. Each PHEV cell has a nominal capacity of 9.5 Ah and a C/3 specific energy of 170 Wh/kg. The BEV cells use $LiFePO_4$(LFP)-coated $LiNi_{0.5}Mn_{0.3}Co_{0.2}O_2$ (NMC532) as cathode materials at a loading of 15.92 mg/cm^2 (90% NMC532 and 10% LFP), or 2.55 mAh/cm^2, and artificial graphite with a BET area of 1.5 m^2/g as anode material at a loading of 8.39 mg/cm^2, or 2.94 mAh/cm^2. Two types of BEV cells are fabricated, one in 10.5 Ah and the other in 35 Ah formats. The 10.5 Ah and 35 Ah BEV cells have a C/3 specific energy of 183 Wh/kg and 209 Wh/kg, respectively. All the cells in this work utilize 1 M $LiPF_6$ dissolved in EC/EMC (3:7 by wt.) + 2 wt % VC as the electrolyte. Detailed design parameters of the cells are listed in Table S1.

All the PHEV and BEV cells adopt the self-heating Li-ion battery structure.[35] Each cell has two pieces of Ni foils embedded inside, as sketched in Figure S3. Each Ni foil has a thickness of 27 μm, a resistance of 98 mΩ at room temperature, a 28-μm-thick polyethylene terephthalate coating layer on each side of the foil for electrical insulation, and is sandwiched between 2 single-sided anode layers. The two 3-layer assemblies are stacked inside the cell, one located at $^1/_4$ cell thickness and the other at $^3/_4$ cell thickness from the top cell surface. One ends of the two Ni foils are welded with the tabs of anode layers and connected to the negative terminal; the other ends

Please cite this article in press as: Yang et al., Asymmetric Temperature Modulation for Extreme Fast Charging of Lithium-Ion Batteries, Joule (2019), https://doi.org/10.1016/j.joule.2019.09.021

of the two Ni foils are welded and extend outside to form a third terminal, the activation terminal.

The added weight and cost due to the introduction of Ni foils are estimated based on the 10.5Ah BEV cells. The added Ni foils weigh 2.7 g, corresponding to 1.3% increase of cell weight and 1.3% drop of gravimetric energy density based on the cell weight of 214 g and the cell energy (at C/3) of 39.16 Wh (Table S1). The cost of the added Ni foils is US$0.83/kWh based on a Ni price of US$12/kg. Assuming a battery cost of US$176/kWh (the average battery cost in 2018 according to Bloomberg[55]), the introduction of Ni foils increases the battery cost by ~0.47%. The durability of Ni foils has been demonstrated in our previous work,[35] where repetitive thermal cycling (heating/cool-down) was performed and minimal degradation was observed.

Cell Test

XFC cycling tests follow the protocols shown in Figures S6–S8 for the PHEV cells and in Figure S18 for the BEV cells, respectively. All tests were conducted at an ambient temperature around 20°C (±2°C). In each XFC cycle, the cells were charged by the heated CCCV protocol at an elevated cell temperature with a constant current of 6 C limited by a cutoff voltage of 4.2 V for the PHEV cells and 4.15 V for the BEV cells to 80% state of charge (SOC) and then discharged at either 1 C or C/3 back to 2.7 V. The C-rates are defined with respect to the nominal cell capacity (9.5 Ah for PHEV cells and 10.5 Ah for BEV cells), and SOC is defined with respect to the remaining cell capacity measured periodically with the reference performance test (RPT). In each RPT, a cell was charged with C/3 rate to 4.2V and then held at 4.2V till the current fell below C/20, rested for 30 min, and then discharged at C/3 rate to 2.7V.

For the baseline cycling tests shown in Figures 6 and 7A, the cells were tested in an environmental chamber at a controlled temperature of 40°C, 50°C, or 60°C. In each cycle, the cells were charged with a constant current of 1 C to 4.2 V (PHEV cells) or 4.15 V (BEV cells) and then held at the cutoff voltage until the current fell below C/3. Thereafter, the cells relaxed for 5 min, discharged at 1 C to 2.7 V, and rested for another 5 min before starting the next cycle.

Post-mortem Characterization

The four PHEV cells after the XFC cycling test (refer to Figure 3B) were fully discharged (C/3 to 2.7 V) and opened in a glove box. The optical photos were taken without washing the electrodes. Samples for SEM imaging and XPS analyses were washed three times with battery-grade ethylmethyl carbonate (EMC) solvent, dried in a vacuum chamber, and transferred into the instrument through a vacuum transfer vessel. SEM images were captured on a Nova NanoSEM 630 instrument. XPS experiments were conducted on a PHI VersaProbe II Scanning XPS Microprobe. XPS depth profiling experiments were performed using a 20 eV Ar^+ beam with a scan area of 20 × 20 μm^2 at a sputtering rate of 30 nm/min based on SiO_2.

SUPPLEMENTAL INFORMATION

Supplemental Information can be found online at https://doi.org/10.1016/j.joule.2019.09.021.

ACKNOWLEDGMENTS

Financial support from the US Department of Energy's Office of Energy Efficiency and Renewable Energy (EERE) under award number DE-EE0008355 is gratefully acknowledged.

Please cite this article in press as: Yang et al., Asymmetric Temperature Modulation for Extreme Fast Charging of Lithium-Ion Batteries, Joule (2019), https://doi.org/10.1016/j.joule.2019.09.021

AUTHOR CONTRIBUTIONS

X.-G.Y. and C.-Y.W. conceived the idea and wrote the manuscript. X.-G.Y. and T.L. designed and carried out the extreme fast charging experiments. Y.G. and D.W. performed SEM and XPS experiments. S.G. and Y.L. performed cycle test of baseline cells. X.-G.Y. and T.L. contributed equally to this work.

DECLARATION OF INTERESTS

The authors declare no competing interests.

Received: June 24, 2019
Revised: July 19, 2019
Accepted: September 26, 2019
Published: October 30, 2019

REFERENCES

1. Needell, Z.A., McNerney, J., Chang, M.T., and Trancik, J.E. (2016). Potential for widespread electrification of personal vehicle travel in the United States. Nat. Energy *1*, 16112.
2. Cano, Z.P., Banham, D., Ye, S., Hintennach, A., Lu, J., Fowler, M., and Chen, Z. (2018). Batteries and fuel cells for emerging electric vehicle markets. Nat. Energy *3*, 279–289.
3. Liu, Y., Zhu, Y., and Cui, Y. (2019). Challenges and opportunities towards fast-charging battery materials. Nat. Energy *4*, 540–550.
4. Howell, D., Boyd, S., Cunningham, B., Gillard, S., Slezak, L., Ahmed, S., Bloom, I., Burnham, A., Hardy, K., Jansen, A.N., et al. (2017). Enabling Fast Charging: a Technology Gap Assessment. No. INL/EXT-17–41638 (U.S. Department of Energy).
5. Nicholas, M., and Hall, D. (2018). Lessons Learned on Early Electric Vehicle Fast-Charging Deployments (International Council on Clean Transportation).
6. Ahmed, S., Bloom, I., Jansen, A.N., Tanim, T., Dufek, E.J., Pesaran, A., Burnham, A., Carlson, R.B., Dias, F., Hardy, K., et al. (2017). Enabling fast charging – a battery technology gap assessment. J. Power Sources *367*, 250–262.
7. Keyser, M., Pesaran, A., Li, Q., Santhanagopalan, S., Smith, K., Wood, E., Ahmed, S., Bloom, I., Dufek, E., Shirk, M., et al. (2017). Enabling fast charging – battery thermal considerations. J. Power Sources *367*, 228–236.
8. Mussa, A.S., Liivat, A., Marzano, F., Klett, M., Philippe, B., Tengstedt, C., Lindbergh, G., Edström, K., Lindström, R.W., and Svens, P. (2019). Fast-charging effects on ageing for energy-optimized automotive LiNi1/3Mn1/3Co1/3O2/graphite prismatic lithium-ion cells. J. Power Sources *422*, 175–184.
9. Tian, R., Park, S.H., King, P.J., Cunningham, G., Coelho, J., Nicolosi, V., and Coleman, J.N. (2019). Quantifying the factors limiting rate performance in battery electrodes. Nat. Commun. *10*, 1933.
10. Tang, Y., Zhang, Y., Li, W., Ma, B., and Chen, X. (2015). Rational material design for ultrafast rechargeable lithium-ion batteries. Chem. Soc. Rev. *44*, 5926–5940.
11. Yao, K.P.C., Okasinski, J.S., Kalaga, K., Shkrob, I.A., and Abraham, D.P. (2019). Quantifying lithium concentration gradients in the graphite electrode of Li-ion cells using operando energy dispersive X-ray diffraction. Energy Environ. Sci. *12*, 656–665.
12. Colclasure, A.M., Dunlop, A.R., Trask, S.E., Polzin, B.J., Jansen, A.N., and Smith, K. (2019). Requirements for enabling extreme fast charging of high energy density Li-Ion cells while avoiding lithium plating. J. Electrochem. Soc. *166*, A1412–A1424.
13. Hall, D.S., Eldesoky, A., Logan, E.R., Tonita, E.M., Ma, X., and Dahn, J.R. (2018). Exploring classes of co-solvents for fast-charging lithium-ion cells. J. Electrochem. Soc. *165*, A2365–A2373.
14. Du, Z., Wood, D.L., and Belharouak, I. (2019). Enabling fast charging of high energy density Li-ion cells with high lithium ion transport electrolytes. Electrochem. Commun. *103*, 109–113.
15. Li, L., Erb, R.M., Wang, J., Wang, J., and Chiang, Y.M. (2019). Fabrication of low-tortuosity ultrahigh-area-capacity battery electrodes through magnetic alignment of emulsion-based slurries. Adv. Energy Mater. *9*, 1802472.
16. Yamada, Y., Yaegashi, M., Abe, T., and Yamada, A. (2013). A superconcentrated ether electrolyte for fast-charging Li-ion batteries. Chem. Commun. (Camb.) *49*, 11194–11196.
17. Yamada, Y., Furukawa, K., Sodeyama, K., Kikuchi, K., Yaegashi, M., Tateyama, Y., and Yamada, A. (2014). Unusual stability of acetonitrile-based superconcentrated electrolytes for fast-charging lithium-ion batteries. J. Am. Chem. Soc. *136*, 5039–5046.
18. Smart, M.C., and Ratnakumar, B.V. (2011). Effects of electrolyte composition on lithium plating in lithium-ion cells. J. Electrochem. Soc. *158*, A379–A389.
19. Kim, N., Chae, S., Ma, J., Ko, M., and Cho, J. (2017). Fast-charging high-energy lithium-ion batteries via implantation of amorphous silicon nanolayer in edge-plane activated graphite anodes. Nat. Commun. *8*, 812.
20. Kim, D.S., Kim, Y.E., and Kim, H. (2019). Improved fast charging capability of graphite anodes via amorphous Al2O3 coating for high power lithium ion batteries. J. Power Sources *422*, 18–24.
21. Sun, Y., Liu, N., and Cui, Y. (2016). Promises and challenges of nanomaterials for lithium-based rechargeable batteries. Nat. Energy *1*, 16071.
22. Son, I.H., Park, J.H., Park, S., Park, K., Han, S., Shin, J., Doo, S.G., Hwang, Y., Chang, H., and Choi, J.W. (2017). Graphene balls for lithium rechargeable batteries with fast charging and high volumetric energy densities. Nat. Commun. *8*, 1561.
23. Li, N., Chen, Z., Ren, W., Li, F., and Cheng, H.M. (2012). Flexible graphene-based lithium ion batteries with ultrafast charge and discharge rates. Proc. Natl. Acad. Sci. USA *109*, 17360–17365.
24. Sun, Y., Wang, L., Li, Y., Li, Y., Lee, H.R., Pei, A., He, X., and Cui, Y. (2019). Design of red phosphorus nanostructured electrode for fast-charging lithium-ion batteries with high energy density. Joule *3*, 1080–1093.
25. Zheng, J., Engelhard, M.H., Mei, D., Jiao, S., Polzin, B.J., Zhang, J.-G., and Xu, W. (2017). Electrolyte additive enabled fast charging and stable cycling lithium metal batteries. Nat. Energy *2*, 17012.
26. Rodrigues, M.-T.F., Babu, G., Gullapalli, H., Kalaga, K., Sayed, F.N., Kato, K., Joyner, J., and Ajayan, P.M. (2017). A materials perspective on Li-ion batteries at extreme temperatures. Nat. Energy *2*, 17108.
27. Yang, X.G., Zhang, G., Ge, S., and Wang, C.Y. (2018). Fast charging of lithium-ion batteries at all temperatures. Proc. Natl. Acad. Sci. USA *115*, 7266–7271.
28. Xu, K., Lam, Y., Zhang, S.S., Jow, T.R., and Curtis, T.B. (2007). Solvation sheath of Li+ in nonaqueous electrolytes and its implication of graphite/electrolyte interface chemistry. J. Phys. Chem. C *111*, 7411–7421.
29. Kulova, T.L., Skundin, A.M., Nizhnikovskii, E.A., and Fesenko, A.V. (2006). Temperature effect on the lithium diffusion rate in graphite. Russ. J. Electrochem *42*, 259–262.

30. Valoen, L.O., and Reimers, J.N. (2005). Transport properties of LiPF6-based Li-Ion battery electrolytes. J. Electrochem. Soc. *152*, A882–A891.

31. Logan, E.R., Tonita, E.M., Gering, K.L., and Dahn, J.R. (2018). A critical evaluation of the advanced electrolyte model. J. Electrochem. Soc. *165*, A3350–A3359.

32. Waldmann, T., Wilka, M., Kasper, M., Fleischhammer, M., and Wohlfahrt-Mehrens, M. (2014). Temperature dependent ageing mechanisms in lithium-ion batteries – A Post-Mortem study. J. Power Sources *262*, 129–135.

33. Yang, X.-G., and Wang, C.-Y. (2018). Understanding the trilemma of fast charging, energy density and cycle life of lithium-ion batteries. J. Power Sources *402*, 489–498.

34. Yang, X.-G., Liu, T., and Wang, C.-Y. (2017). Innovative heating of large-size automotive Li-ion cells. J. Power Sources *342*, 598–604.

35. Wang, C.Y., Zhang, G., Ge, S., Xu, T., Ji, Y., Yang, X.G., and Leng, Y. (2016). Lithium-ion battery structure that self-heats at low temperatures. Nature *529*, 515–518.

36. von Lüders, C., Zinth, V., Erhard, S.V., Osswald, P.J., Hofmann, M., Gilles, R., and Jossen, A. (2017). Lithium plating in lithium-ion batteries investigated by voltage relaxation and in situ neutron diffraction. J. Power Sources *342*, 17–23.

37. Yang, X.-G., Ge, S., Liu, T., Leng, Y., and Wang, C.-Y. (2018). A look into the voltage plateau signal for detection and quantification of lithium plating in lithium-ion cells. J. Power Sources *395*, 251–261.

38. Campbell, I.D., Marzook, M., Marinescu, M., and Offer, G.J. (2019). How observable is lithium plating? Differential voltage analysis to identify and quantify lithium plating following fast charging of cold lithium-ion batteries. J. Electrochem. Soc. *166*, A725–A739.

39. Gao, Y., Yan, Z., Gray, J.L., He, X., Wang, D., Chen, T., Huang, Q., Li, Y.C., Wang, H., Kim, S.H., et al. (2019). Polymer–inorganic solid–electrolyte interphase for stable lithium metal batteries under lean electrolyte conditions. Nat. Mater. *18*, 384–389.

40. Maire, P., Evans, A., Kaiser, H., Scheifele, W., and Novák, P. (2008). Colorimetric determination of lithium content in electrodes of lithium-ion batteries. J. Electrochem. Soc. *155*, A862–A865.

41. Verma, P., Maire, P., and Novák, P. (2010). A review of the features and analyses of the solid electrolyte interphase in Li-ion batteries. Electrochim. Acta *55*, 6332–6341.

42. Gao, Y., Zhao, Y., Li, Y.C., Huang, Q., Mallouk, T.E., and Wang, D. (2017). Interfacial chemistry regulation via a skin-grafting strategy enables high-performance lithium-metal batteries. J. Am. Chem. Soc. *139*, 15288–15291.

43. Gao, Y., Yi, R., Li, Y.C., Song, J., Chen, S., Huang, Q., Mallouk, T.E., and Wang, D. (2017). General method of manipulating formation, composition, and morphology of solid-electrolyte interphases for stable Li-alloy anodes. J. Am. Chem. Soc. *139*, 17359–17367.

44. Ploehn, H.J., Ramadass, P., and White, R.E. (2004). Solvent diffusion model for aging of lithium-ion battery cells. J. Electrochem. Soc. *151*, A456–A462.

45. Pinson, M.B., and Bazant, M.Z. (2013). Theory of SEI formation in rechargeable batteries: capacity fade, accelerated aging and lifetime prediction. J. Electrochem. Soc. *160*, A243–A250.

46. Smith, A.J., Burns, J.C., Zhao, X., Xiong, D., and Dahn, J.R. (2011). A high precision coulometry study of the SEI growth in Li/graphite cells. J. Electrochem. Soc. *158*, A447–A452.

47. Burns, J.C., Stevens, D.A., and Dahn, J.R. (2015). In-situ detection of lithium plating using high precision coulometry. J. Electrochem. Soc. *162*, A959–A964.

48. Schuster, S.F., Bach, T., Fleder, E., Müller, J., Brand, M., Sextl, G., and Jossen, A. (2015). Nonlinear aging characteristics of lithium-ion cells under different operational conditions. J. Energy Storage *1*, 44–53.

49. Yang, X.-G., Leng, Y., Zhang, G., Ge, S., and Wang, C.-Y. (2017). Modeling of lithium plating induced aging of lithium-ion batteries: transition from linear to nonlinear aging. J. Power Sources *360*, 28–40.

50. Jung, R., Metzger, M., Maglia, F., Stinner, C., and Gasteiger, H.A. (2017). Oxygen release and its effect on the cycling stability of LiNixMnyCozO2 (NMC) cathode materials for Li-Ion batteries. J. Electrochem. Soc. *164*, A1361–A1377.

51. Ma, X., Harlow, J.E., Li, J., Ma, L., Hall, D.S., Buteau, S., Genovese, M., Cormier, M., and Dahn, J.R. (2019). Hindering rollover failure of Li. J. Electrochem. Soc. *166*, A711–A724.

52. Average annual miles of American drivers, by U.S. Department of Transportation Federal Highway Administration. https://www.fhwa.dot.gov/ohim/onh00/bar8.htm04/25.

53. Wu, Z., Ji, S., Liu, T., Duan, Y., Xiao, S., Lin, Y., Xu, K., and Pan, F. (2016). Aligned Li+ tunnels in core–shell Li(NixMnyCoz)O2@LiFePO4 enhances its high voltage cycling stability as Li-ion battery cathode. Nano Lett. *16*, 6357–6363.

54. Zhu, L., Yan, T.-F., Jia, D., Wang, Y., Wu, Q., Gu, H.-T., Wu, Y.-M., et al. (2019). LiFePO4-coated LiNi0.5Co0.2Mn0.3O2 cathode materials with improved high voltage electrochemical performance and enhanced safety for lithium ion pouch cells. J. Electrochem. Soc. *166*, A5437–A5444.

55. Electric vehicle Outlook 2019, Bloomberg NEF. https://about.bnef.com/electric-vehicle-outlook/.

JOUL, Volume *3*

Supplemental Information

Asymmetric Temperature Modulation for Extreme Fast Charging of Lithium-Ion Batteries

Xiao-Guang Yang, Teng Liu, Yue Gao, Shanhai Ge, Yongjun Leng, Donghai Wang, and Chao-Yang Wang

Table S1. Cell design information of the PHEV and BEV pouch cells in this work.

		9.5 Ah PHEV cell	10.5 Ah BEV cell	35 Ah BEV cell
Anode	Active material	Artificial Graphite	Artificial Graphite	Artificial Graphite
	BET area	3.9 m^2/g	1.5 m^2/g	1.5 m^2/g
	Mass Loading	6.68 mg/cm^2	8.39 mg/cm^2	8.39 mg/cm^2
	Areal capacity	2.33 mAh/cm^2	2.94 mAh/cm^2	2.94 mAh/cm^2
	Cu foil thickness	10 μm	8 μm	8 μm
	Dimension	123×72 mm	123×72 mm	196×154 mm
	Number of layers	34	27	24
Cathode	Active material	$LiNi_{0.6}Mn_{0.2}Co_{0.2}O_2$	$LiFePO_4$-coated $LiNi_{0.5}Mn_{0.3}Co_{0.2}O_2$	$LiFePO_4$-coated $LiNi_{0.5}Mn_{0.3}Co_{0.2}O_2$
	Mass Loading	10.57 mg/cm^2	15.92 mg/cm^2	15.92 mg/cm^2
	Areal capacity	1.85 mAh/cm^2	2.55 mAh/cm^2	2.55 mAh/cm^2
	Al foil thickness	15 μm	15 μm	15 μm
	Dimension	120×69 mm	120×69 mm	192×151 mm
	Number of layers	33	26	23
Electrolyte		1M $LiPF_6$ dissolved in EC/EMC (3:7 by wt.)+2wt% VC		
Separator		Celgard-2325 microporous tri-layer membrane		
Weight		208 g	214 g	619 g
Capacity		9.5 Ah	10.5 Ah	35 Ah
Specific Energy	C/10	175 Wh/kg	190 Wh/kg	217 Wh/kg
	C/3	170 Wh/kg	183 Wh/kg	209 Wh/kg
	1C	162 Wh/kg	172 Wh/kg	196 Wh/kg

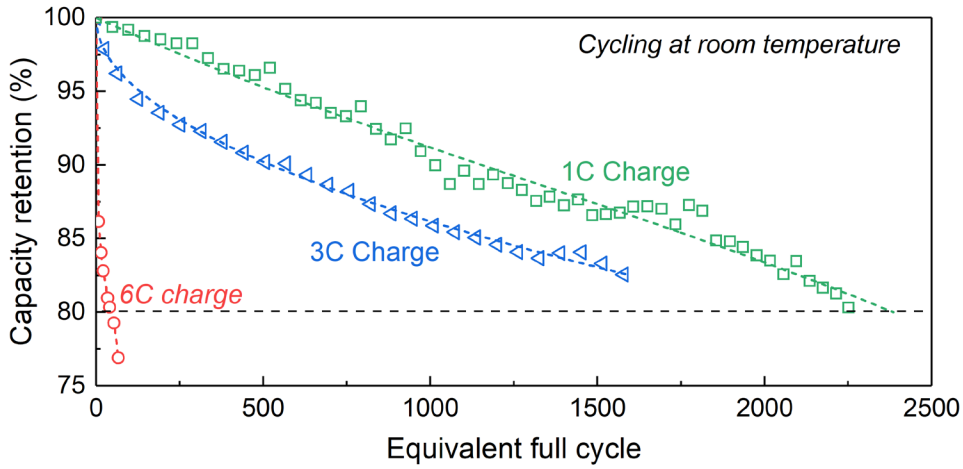

Figure S1. **Drastic drop of cell life under 6C extreme fast charging.** Capacity retention of the baseline PHEV cells cycled with different charge rates. All cells were tested at room temperature.

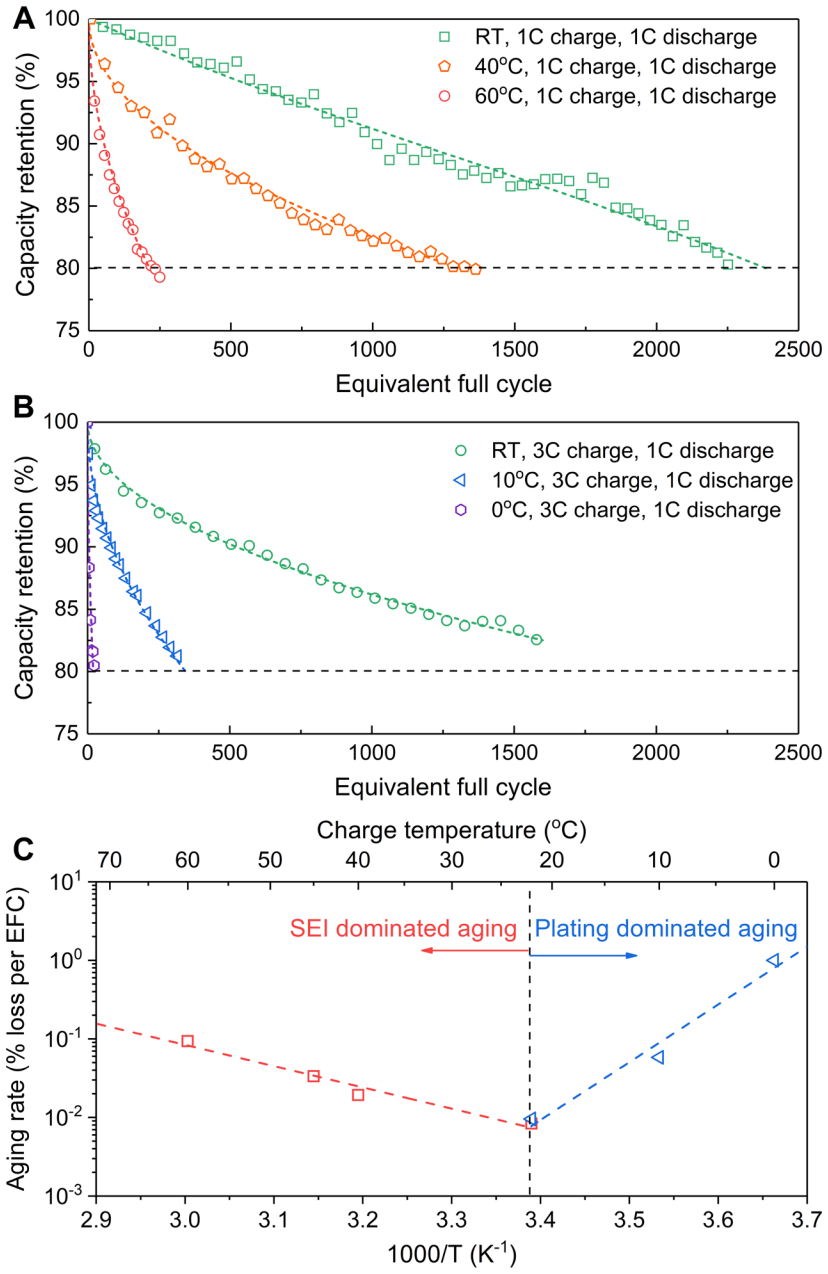

Figure S2. The dilemma of Li plating and solid electrolyte interphase (SEI) growth. Increase of temperature alleviates Li plating but accelerates SEI growth. The cell reaches an optimum life at around room temperature (RT). **(A&B)** Capacity retention vs equivalent full cycle (EFC) of the PHEV cells cycled with **(A)** 1C charge and 1C discharge at RT, 40°C and 60°C, respectively, and **(B)** 3C charge and 1C discharge at RT, 10°C and 0°C, respectively. **(C)** Summary of aging rate (capacity loss in % per EFC) versus reciprocal temperature of the cells in **(A)** and **(B)**.

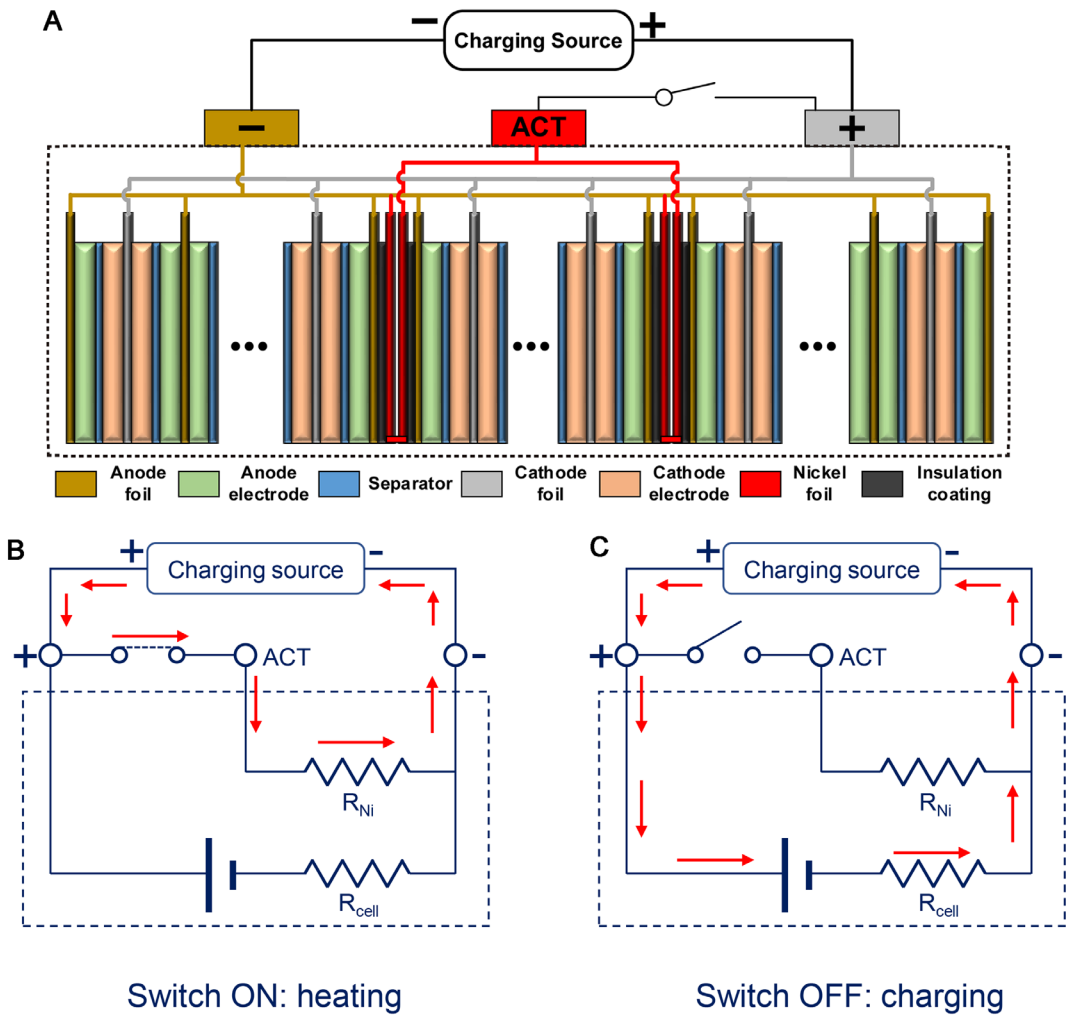

Figure S3. Working principle of the heated-charge approach with self-heating Li-ion battery structure. (A) Schematic of the self-heating Li-ion battery structure utilized in this work. Two pieces of thin nickel (Ni) foils are embedded inside the cell, one located at ¼ cell thickness from the cell surface and the other at ¾ cell thickness. Each Ni foil is coated with polyethylene terephthalate layers for electrical insulation and sandwiched between 2 single-sided anode layers. One ends of the two Ni foils are welded with anode tables and connected to the negative terminal; the other ends extend outside the cell to form the so-called activation (ACT) terminal. A switch is added between positive and ACT terminals. **(B&C)** Flow of current during the **(B)** heating and **(C)** charging steps. In **(B)**, the current is fed to the cell along with closing the switch between positive and ACT terminals. The product of input current I and Ni foil resistance R_{Ni} is close to cell open-circuit voltage; thus all the current flows into the Ni foils without charging battery materials in the heating step. Once cell temperature reaches a defined value, the switch is opened, as in **(C)**, and the cell is reverted to a conventional cell and is charged with the conventional charge method.

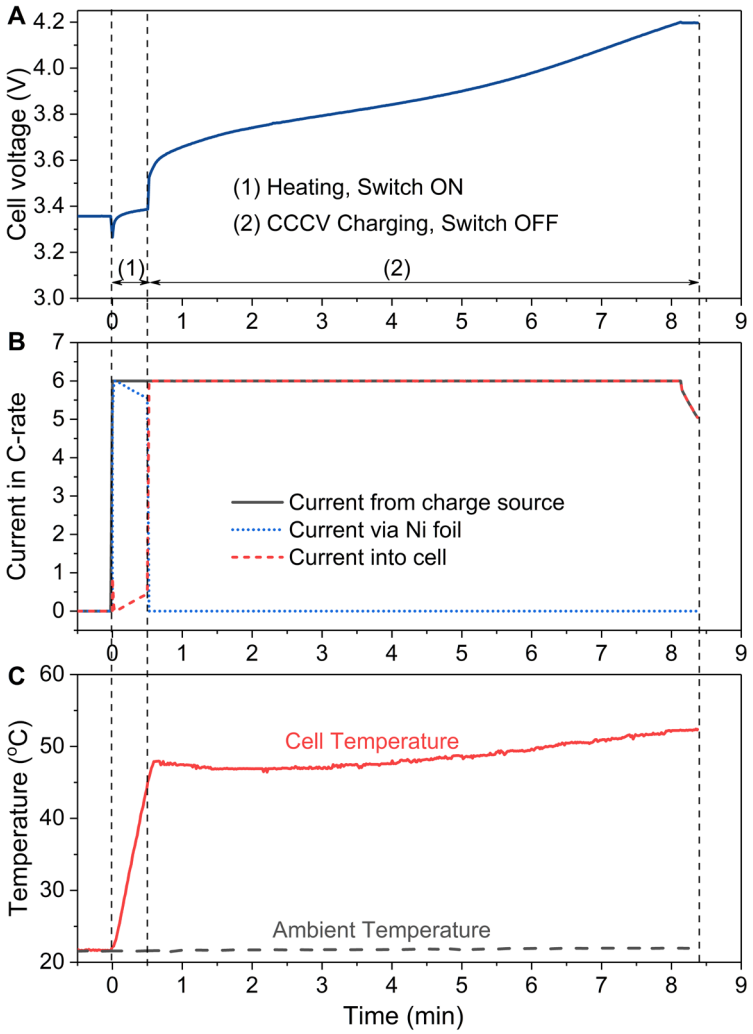

Figure S4. The heated constant-current constant-voltage charge protocol. Evolutions of **(A)** cell voltage, **(B)** current, and **(C)** temperature in a heated-CCCV charge process. Step (1) refers to heating and (2) to CCCV charging. During the heating step, the switch (see Figure S3) is closed and most of the input current from the charging source (solid black line in **B**) goes into the Ni foils inside the cell (dotted blue line in **B**). Once cell temperature reaches a defined value (45°C in this case), the switch is opened and the cell is charged with the 6C current limited by a 4.2V cutoff voltage until reaching 80% state of charge. The cell stays at a high temperature in the charge step, as in **C**, though the cell was tested in ambient air at ~21°C without any forced convection.

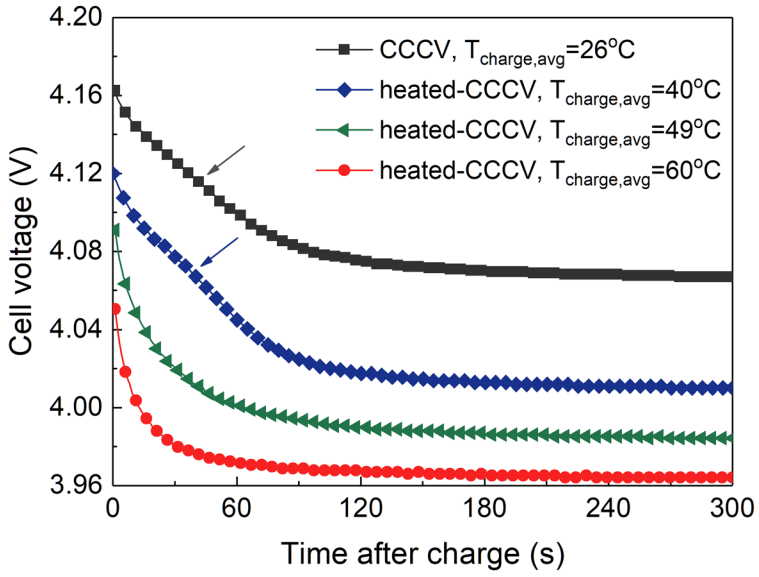

Figure S5. Voltage relaxation curve after extreme fast charging. Evolution of cell voltage in the rest step subsequent to the CCCV (6C, 4.2V) charge to 80% SOC at different average charge temperatures (refer to Figure 2A). The voltage plateau (marked by the arrows) of the 26ºC and 40ºC cases indicate stripping of plated Li metal.

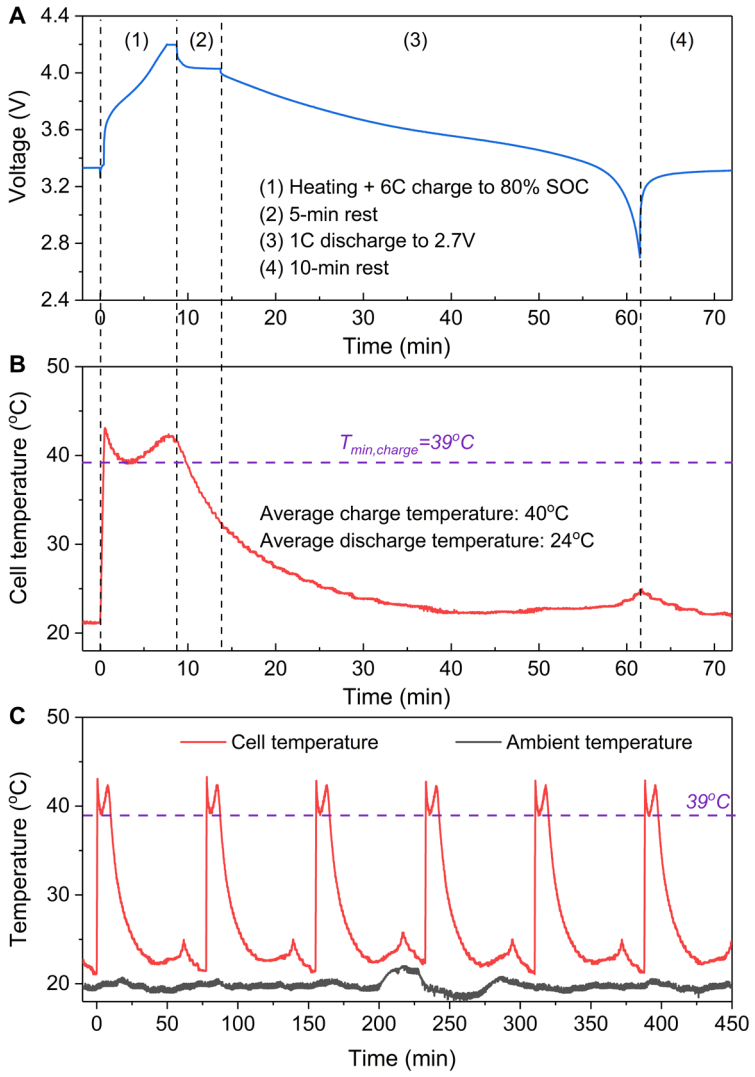

Figure S6. The XFC cycling protocol of the PHEV cell with heated-charge at ~40°C. (A&B) Evolutions of **(A)** cell voltage, and **(B)** cell temperature in a complete extreme fast charge (XFC) cycle with asymmetric temperature modulation. The cell was tested at an ambient temperature around 20°C. The whole cycle includes: a heating step to warm up the cell, CCCV (6C, 4.2V) charge to 80% state of charge (SOC), 5-min rest after charge, 1C discharge back to 2.7V, 10-min rest after discharge. The minimum and average cell temperature in the charge step is 39°C and 40°C, respectively. **(C)** Evolutions of cell temperature in six consecutive XFC cycles. The time during which cell temperature is >39°C is utilized for plotting capacity retention vs time in Figure 6A.

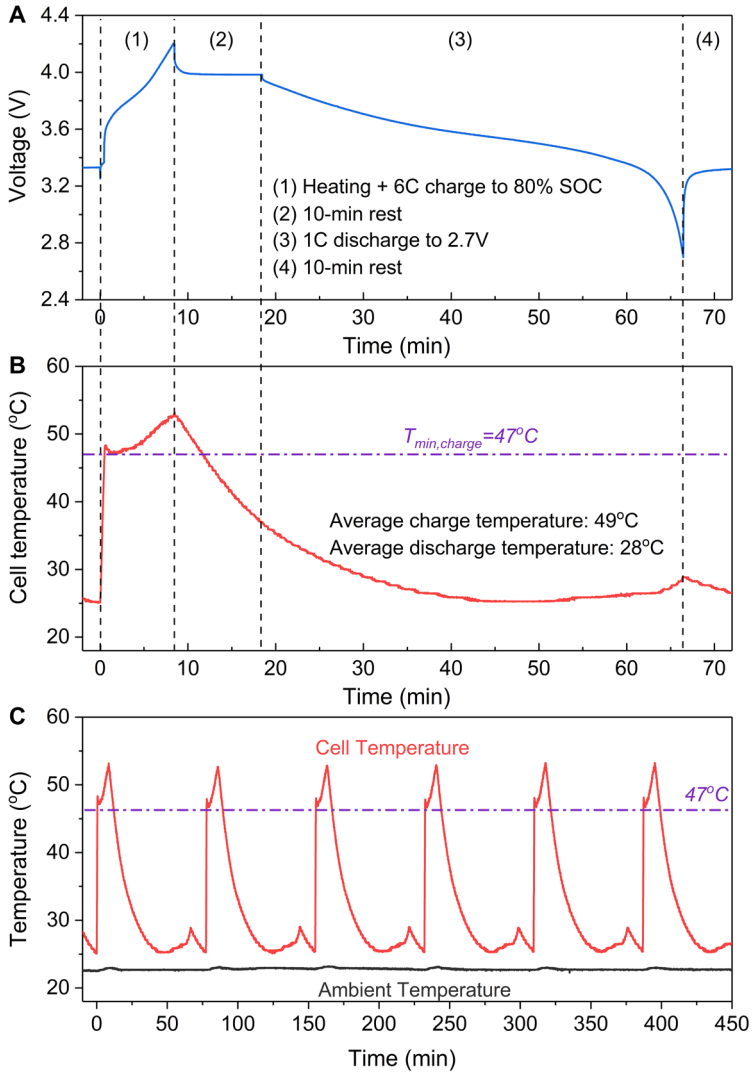

Figure S7. The XFC cycling protocol of the PHEV cell with heated-charge at ~49°C. (A&B) Evolutions of **(A)** cell voltage, and **(B)** cell temperature in a complete extreme fast charge (XFC) cycle with asymmetric temperature modulation. The cell was tested at an ambient temperature around 22°C. The whole cycle includes: a heating step to warm up the cell, CCCV (6C, 4.2V) charge to 80% state of charge (SOC), 10-min rest after charge, 1C discharge back to 2.7V, 10-min rest after discharge. The minimum and average cell temperature in the charge step is 47°C and 49°C, respectively. **(C)** Evolutions of cell temperature in six consecutive XFC cycles. The time during which cell temperature is >47°C is utilized for plotting capacity retention vs time in Figure 6B.

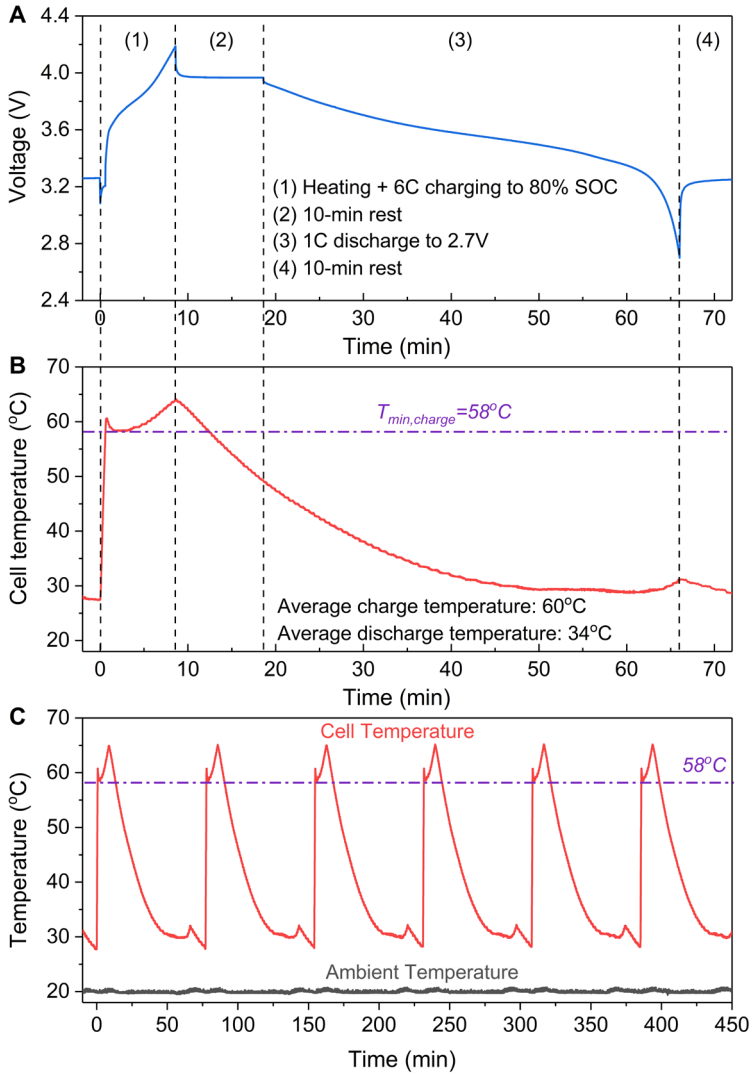

Figure S8. The XFC cycling protocol of the PHEV cell with heated-charge at ~60°C. (A&B) Evolutions of **(A)** cell voltage, and **(B)** cell temperature in a complete extreme fast charge (XFC) cycle with asymmetric temperature modulation. The cell was tested at an ambient temperature around 20°C. The whole cycle includes: a heating step to warm up the cell, CCCV (6C, 4.2V) charge to 80% state of charge (SOC), 10-min rest after charge, 1C discharge back to 2.7V, 10-min rest after discharge. The minimum and average cell temperature in the charge step is 58°C and 60°C, respectively. **(C)** Evolutions of cell temperature in six consecutive XFC cycles. The time during which cell temperature is >58°C is utilized for plotting capacity retention vs time in Figure 6C.

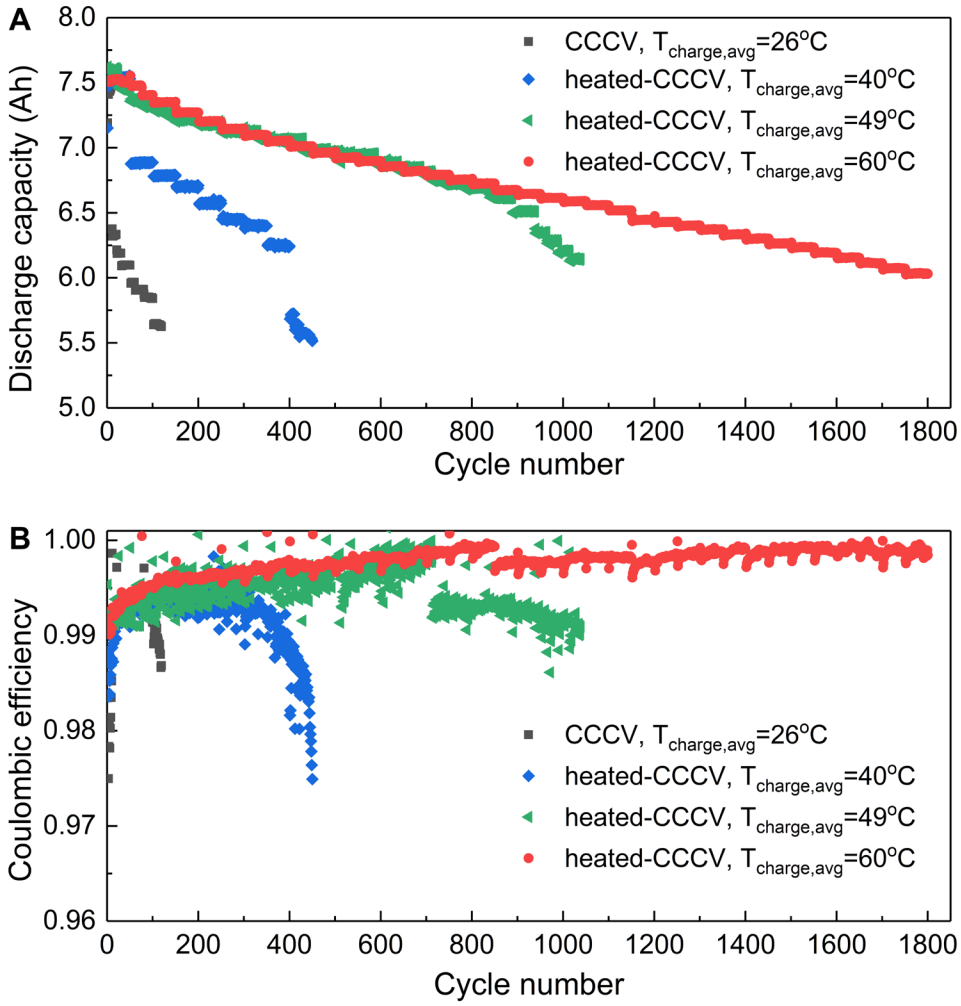

Figure S9. Discharge capacity and coulombic efficiency during XFC cycling. Evolutions of **(A)** 1C discharge capacity, and **(B)** coulombic efficiency, of the four PHEV cells in the XFC cycling process at different average charge temperatures.

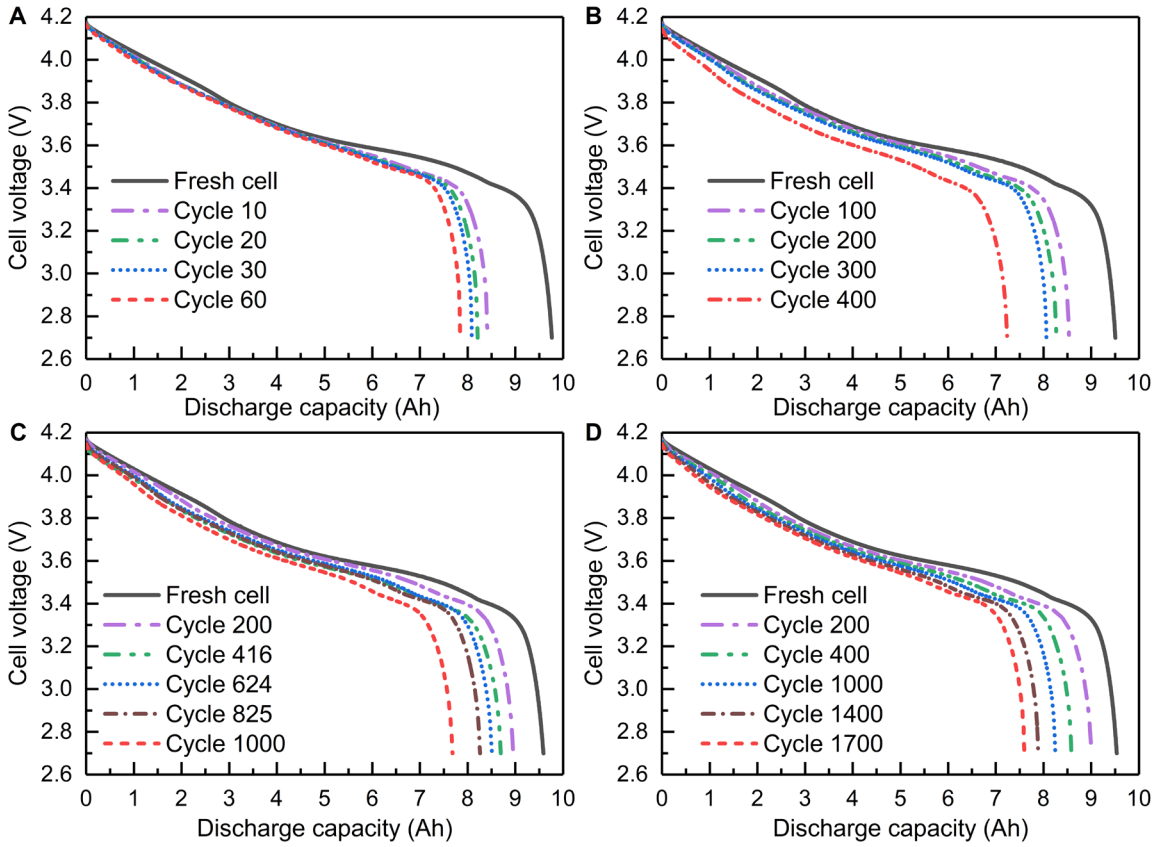

Figure S10. C/3 discharge curves of fresh and aged PHEV cells measured in the reference performance tests (RPTs). In each RPT, the cell is charged with C/3 rate to 4.2V and then held at 4.2V till the current falls below C/20, rests for 30 minutes, and then discharges at C/3 rate to 2.7V. **(A)-(D)** refer to the four PHEV cells presented in Figures 2-6, which are cycled with 6C charge limited by 4.2V to 80% SOC at an average charge temperature of **(A)** 26°C, **(B)** 40°C, **(C)** 49°C and **(D)** 60°C, respectively.

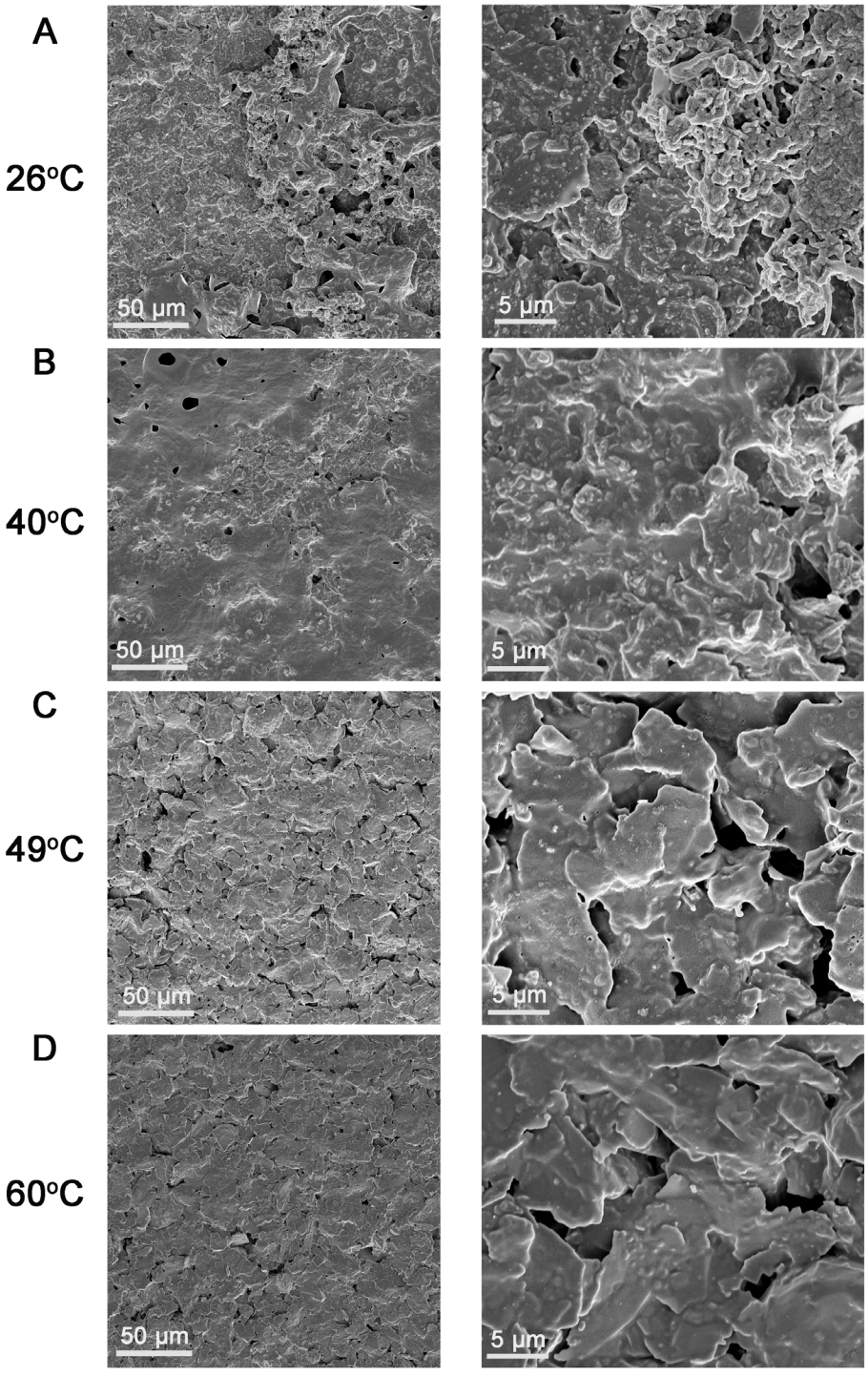

Figure S11 SEM images showing mitigated Li plating at elevated charge temperatures. SEM images of the aged anodes in the four PHEV cells after XFC cycling at different average charge temperatures: (A) 26°C, (B) 40°C, (C) 49°C, and (D) 60°C. The SEM samples are taken from the center region of the anode layers (refer to Figure 3C-F).

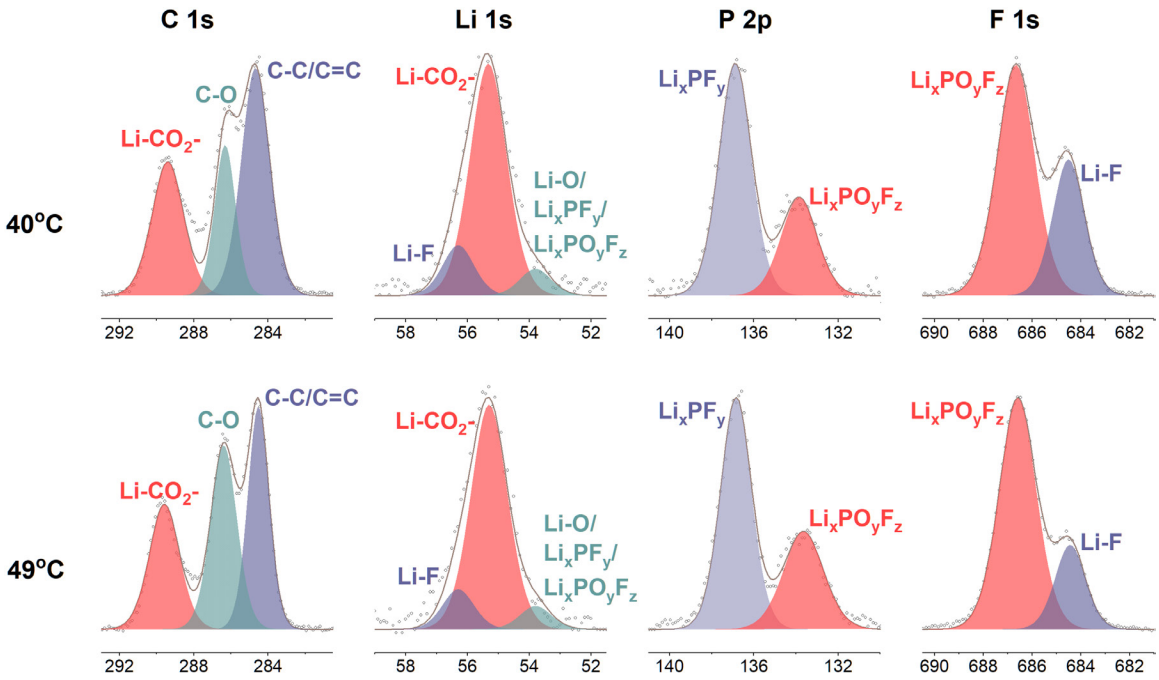

Figure S12. SEI composition at elevated charge temperatures. High-resolution XPS spectra of C 1s, Li 1s, P 2p, F 1s of the aged anodes from the PHEV cells after the XFC cycling test at the average charge temperature of 40°C and 49°C (refer to Figure 3B).

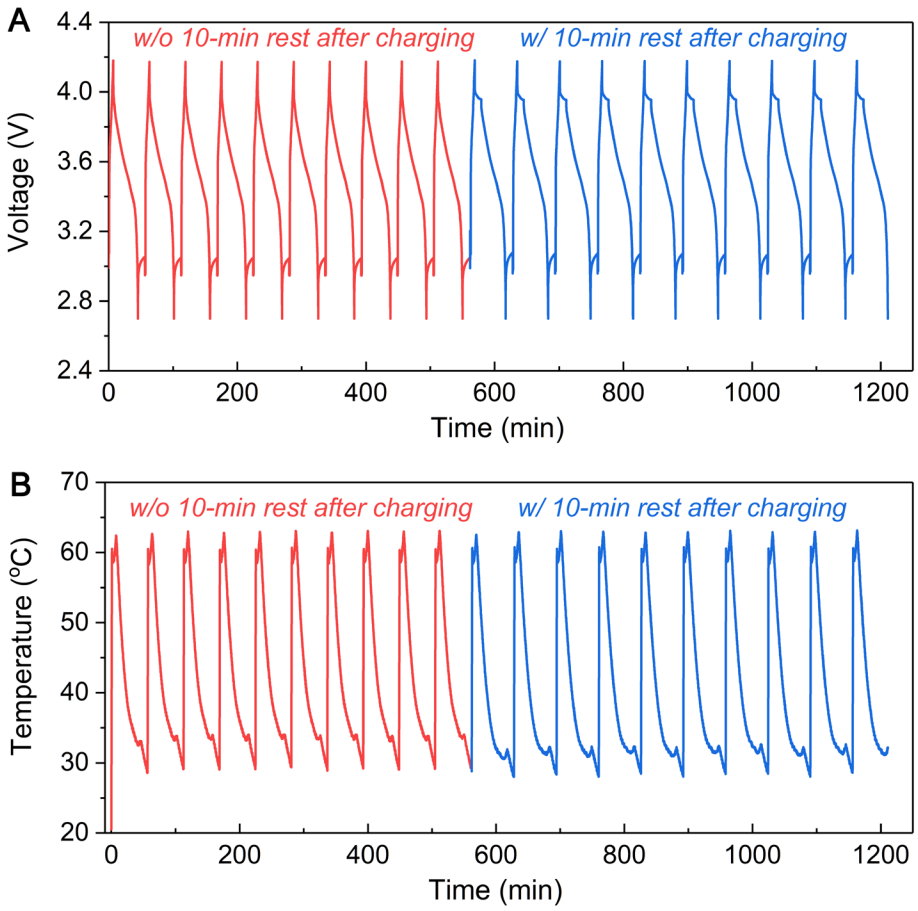

Figure S13. Voltage and temperature evolutions with and without a rest step after charging. The test was done with the aged PHEV cell after 1,800 XFC cycles with the heated-charge at 60°C (refer to Fig. 3B). In this test, 20 consecutive XFC cycles were conducted with the heated-CCCV (6C, 4.2V) charge at 60°C and 1C discharge. The first 10 cycles had no rest step after the 6C charge to 80% SOC, and the second 10 cycles had a 10-min rest step after the 6C charge.

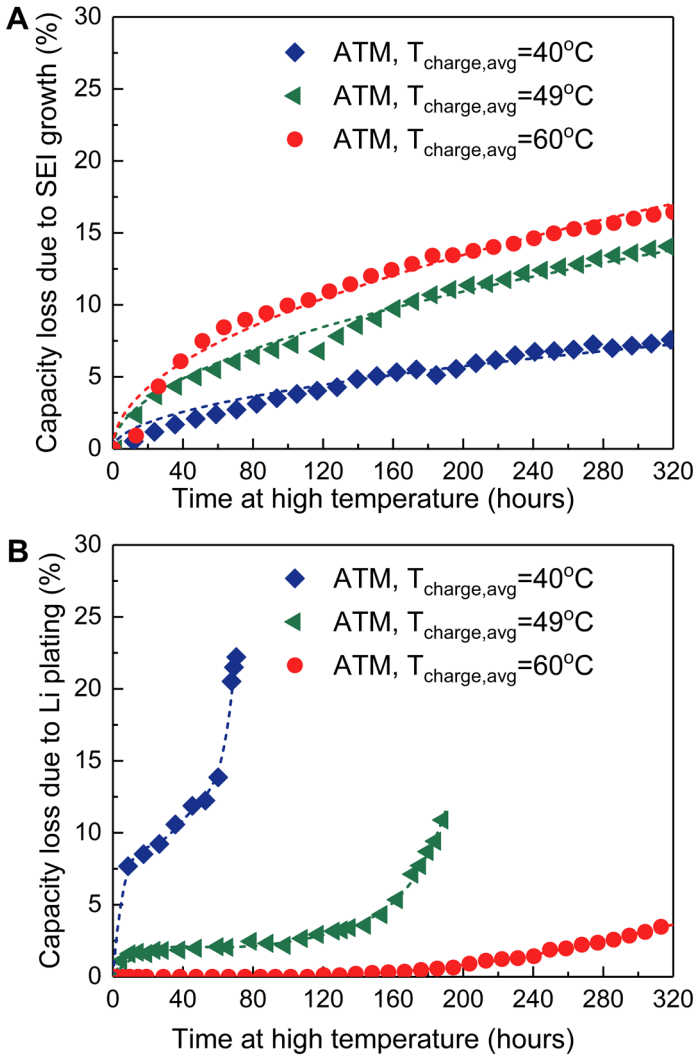

Figure S14. Contributions of SEI growth and Li plating to the total capacity loss of the PHEV cells with asymmetric temperature modulation (ATM). The overall capacity loss induced by SEI growth in **(A)** is calculated by the capacity loss of the baseline cells in Figure 6A-6C, which are cycled with 1C charge and 1C discharge at a controlled temperature of 40°C, 50°C and 60°C, respectively. The capacity loss due to Li plating in **(B)** is estimated by the difference in capacity retention between the ATM and baseline cells in Figure 6A-6C. The ATM cells are cycled with 6C charge at an elevated temperature and 1C discharge at around room temperature.

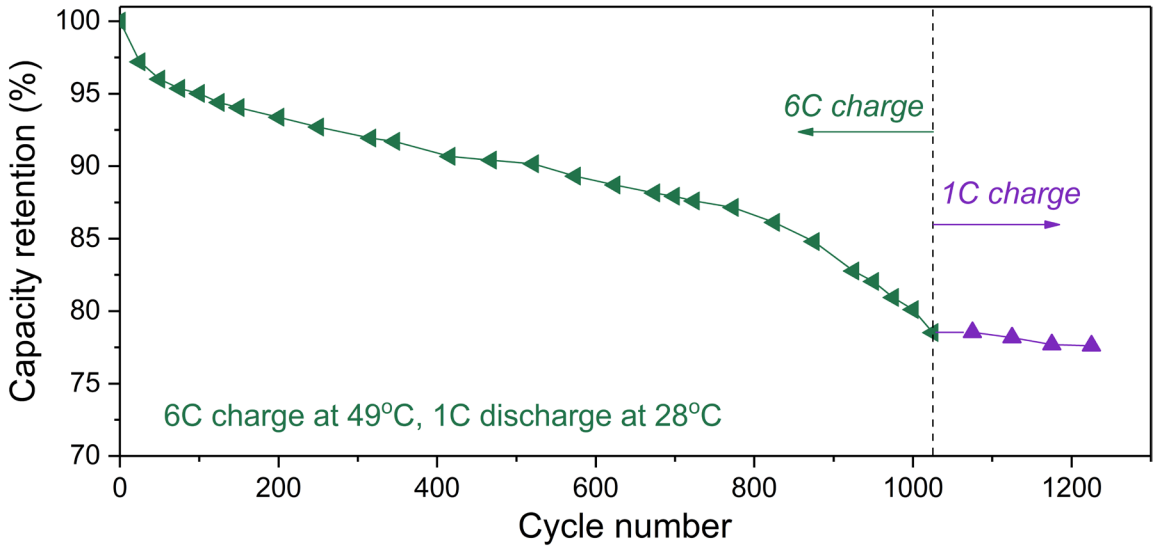

Figure S15. Capacity rollover is strongly affected by charge rate. The PHEV cell cycled with 6C charge at an average cell temperature of 49°C (refer to Figure 3B) switched to cycling with 1C charge and 1C discharge at room temperature after 1025 extreme fast charge cycles, and capacity retention immediately stabilized.

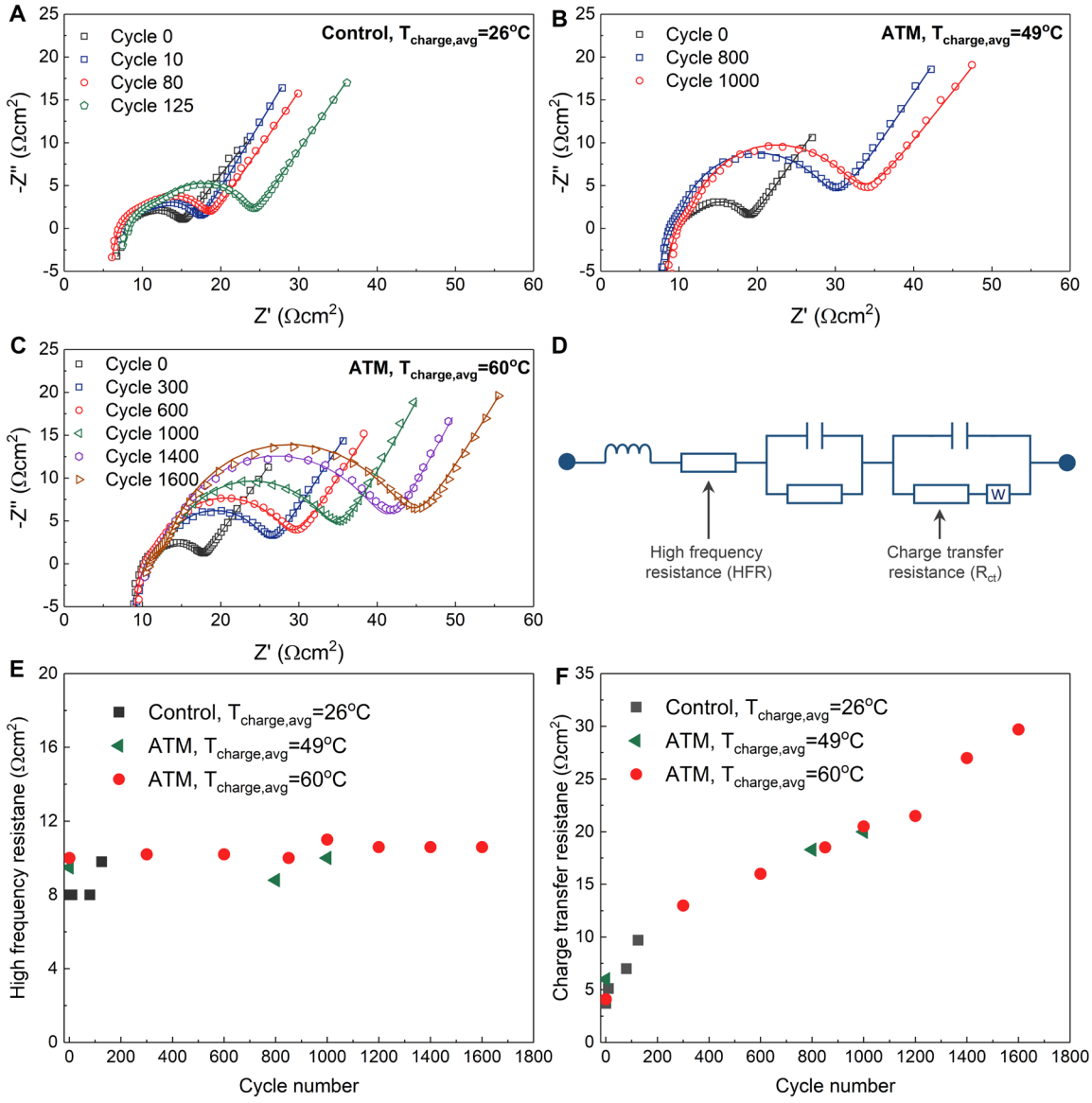

Figure S16. Evolution of cell impedance during XFC cycling with asymmetric temperature modulation (ATM). (A-C) Impedance spectra of the PHEV cells cycled with 6C charge at an average charge temperature of **(A)** 26°C, **(B)** 49°C, and **(C)** 60°C. **(D)** The equivalent circuit used for fitting the impedance spectra. **(E&F)** Evolution of the fitted **(E)** high frequency resistance and **(F)** charge transfer resistance of the three PHEV cells during cycling.

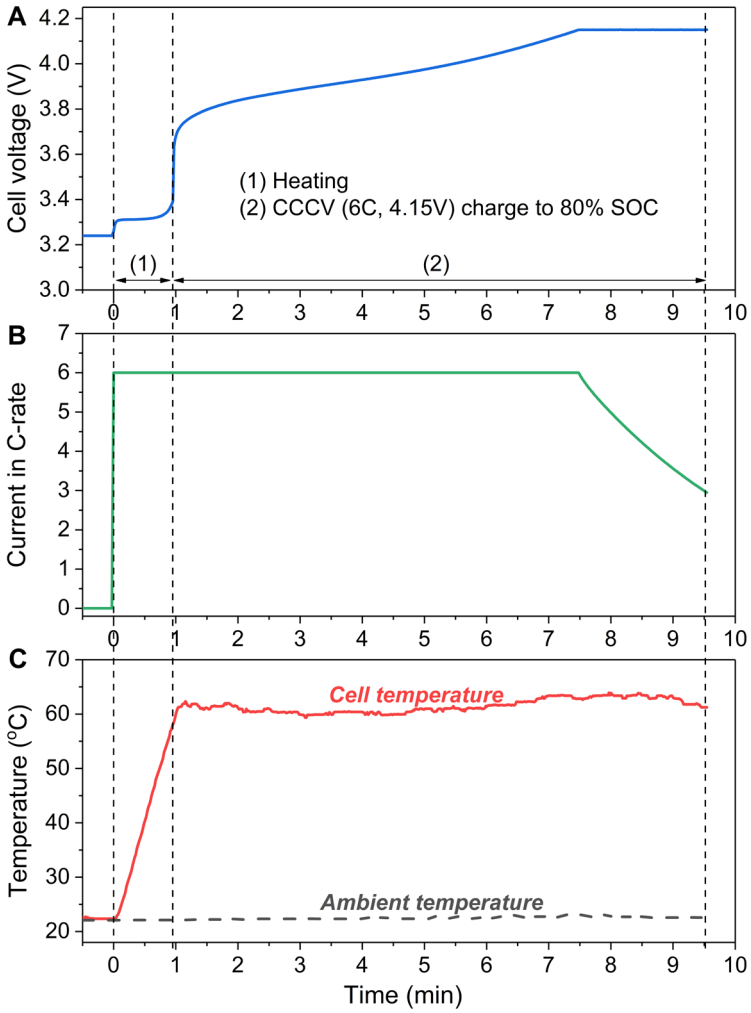

Figure S17. 10-min extreme fast charging of the high-energy BEV cell. Evolutions of **(A)** cell voltage, **(B)** current, and **(C)** temperature in the heated constant-current constant-voltage charge process of the 10.5 Ah BEV cell.

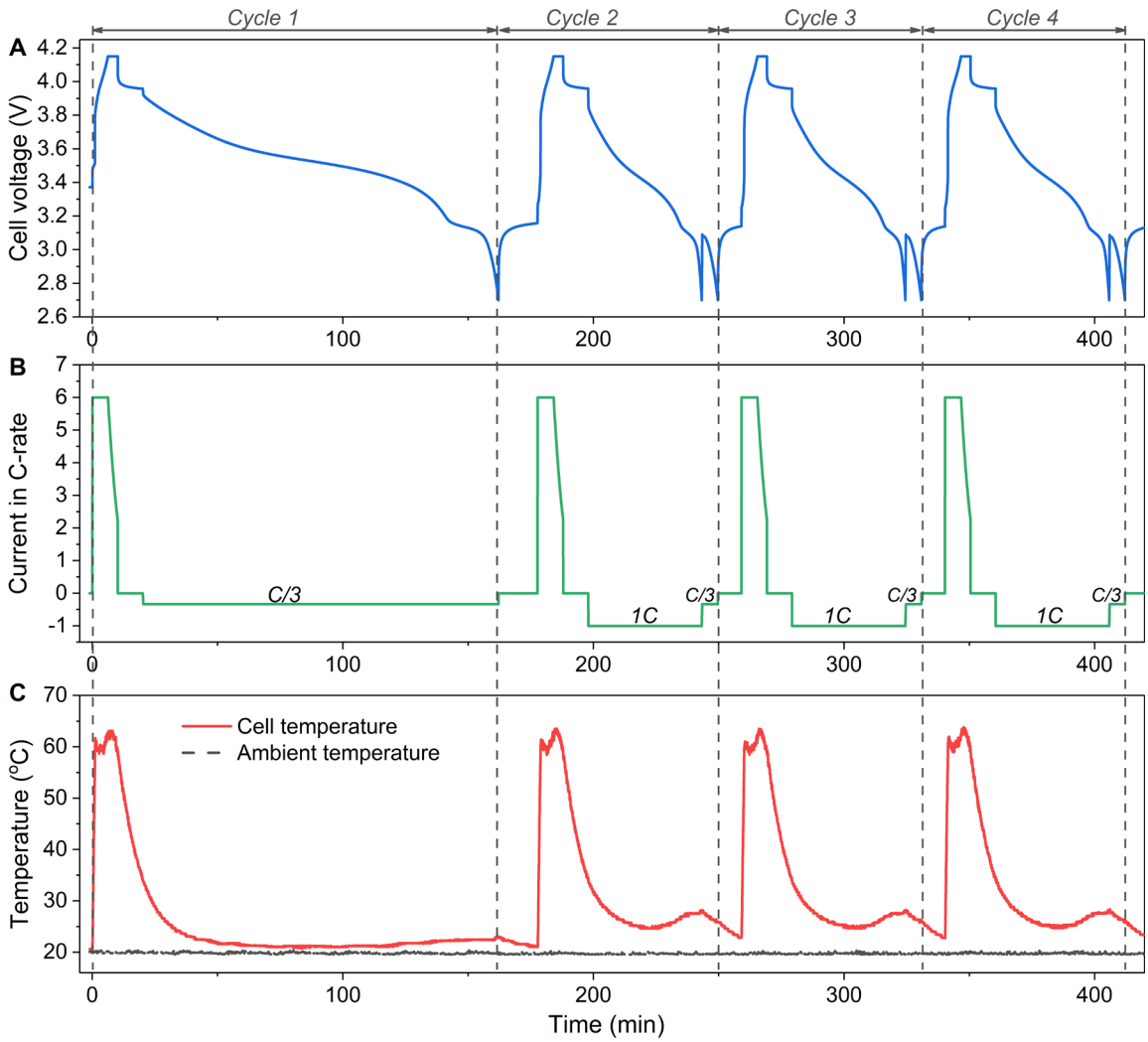

Figure S18. The XFC cycling protocol of the high-energy BEV cell. Evolutions of **(A)** cell voltage, **(B)** current, and **(C)** temperature in four consecutive extreme fast charge (XFC) cycles of the BEV cell. In the first XFC cycle of each 50 consecutive XFC cycles, the cell charged to 80% state of charge (SOC) is discharged at C/3 rate to 2.7V. In the remainder 49 XFC cycles, the cell after charging to 80% SOC is first discharged at 1C to 2.7V followed by a second discharge at C/3 to 2.7V (see **B**) to save the total test time. The cycling test was paused every 50 consecutive XFC cycles for calibration of capacity fade.

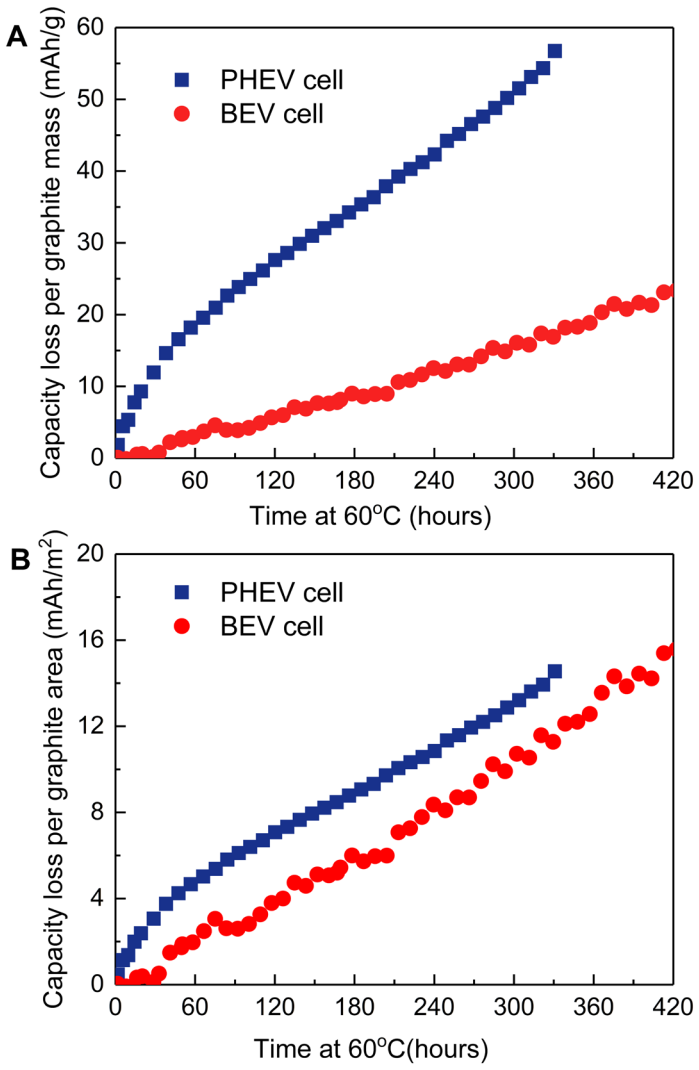

Figure S19. Importance of graphite specific surface area on SEI-induced capacity loss. Comparison of the capacity loss, normalized by **(A)** total graphite mass, and **(B)** total graphite surface area, respectively, of the PHEV and BEV cells in the time domain. The graphite mass and surface area refer to effective graphite (within the dimension of the corresponding cathodes, excluding overhang regions). The PHEV and BEV cells become fairly close to each other when the capacity losses are normalized by graphite surface area (see **B**).

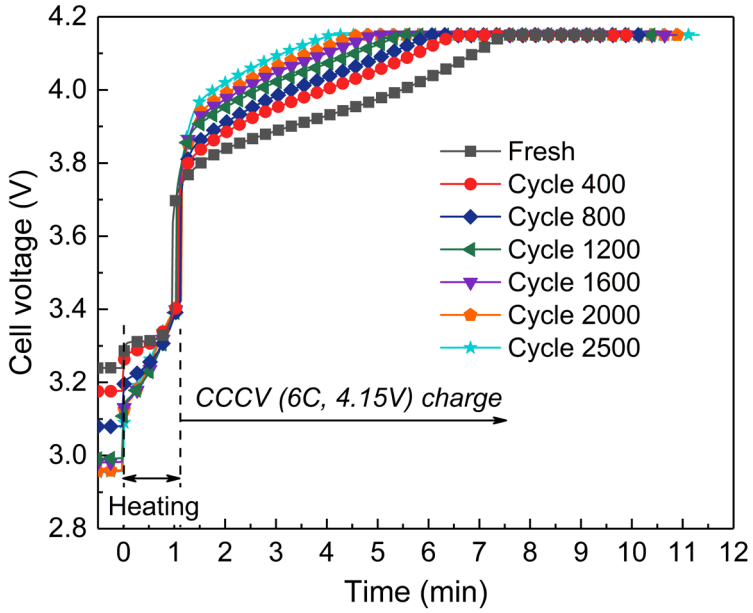

Figure S20. Charge curves of the fresh and aged BEV cells. Cell resistance increases over cycling which leads to a longer constant voltage charge period. Nevertheless, the cell can still be charged to 80% state of charge in 11.6 minutes after 2,500 XFC cycles.